https://doi.org/10.5194/egusphere-2024-2193
Preprint. Discussion started: 30 July 2024

Estimation of the radiation budget during MOSAiC based on ground-based and satellite remote sensing observations

Carola Barrientos-Velasco[1], Christopher J. Cox[2], Hartwig Deneke[1], J. Brant Dodson[3], Anja Hünerbein[1], Matthew D. Shupe[2,4], Patrick C. Taylor[5], and Andreas Macke[1]

[1]Leibniz Institute for Tropospheric Research, Leipzig, Germany
[2]NOAA, Physical Sciences Laboratory, Boulder, Colorado, USA
[3]Science Systems and Applications, Inc., Hampton, VA 23666, USA
[4]Cooperative Institute for Research in Environmental Sciences, University of Colorado, Boulder, Colorado, USA
[5]NASA Langley Research Center, Hampton, VA, USA

Correspondence: Carola Barrientos-Velasco (barrientos@tropos.de)

Abstract. An accurate representation of the radiation budget is essential for investigating the radiative effect that clouds have on the climate system, especially in the Arctic, an environment highly sensitive to complex and rapid environmental changes. In this study, we analyse a unique dataset of observations from the central Arctic made during the MOSAiC (Multidisciplinary drifting Observatory for the Study of Arctic Climate) expedition in conjunction with state-of-the-art satellite products from CERES (Clouds and the Earth's Radiant Energy System) to investigate the radiative effect of clouds and radiative closure at the surface and the top of the atmosphere (TOA). We perform a series of radiative transfer simulations using derived cloud macro- and microphysical properties as inputs to the simulations for the entire MOSAiC period, comparing our results to collocated satellite products and ice-floe observations. The radiative closure biases were generally within the instrumental uncertainty, indicating that the simulations are sufficiently accurate to realistically reproduce the radiation budget during MOSAiC. Comparisons of the simulated radiation budget relative to CERES show similar values in the terrestrial flux but relatively large differences in the solar flux, which is attributed to a lower surface albedo and a possible underestimation of atmospheric opacity by CERES. While the simulation results were consistent with the observations, more detailed analyses reveal an overestimation of simulated cloud opacity for cases involving geometrically thick ice clouds. In the annual mean, we found that the presence of clouds leads to a loss of 5.2 $\mathrm{W\,m^{-2}}$ of the atmospheric-surface system to space, while the surface gains 25 $\mathrm{W\,m^{-2}}$, and the atmosphere is cooled by clouds by 30.2 $\mathrm{W\,m^{-2}}$ during the MOSAiC expedition.

1 Introduction

In recent decades, the Arctic has undergone one of the most rapid changes in climate and ecosystem dynamics on Earth (Serreze and Barry, 2011). Characterised by its unique climatic conditions, the warming in the Arctic region is considered a

https://doi.org/10.5194/egusphere-2024-2193
Preprint. Discussion started: 30 July 2024

robust feature of climate change (Meredith et al., 2019). Among the various factors influencing the Arctic climate, clouds have emerged as critical and important components that play a crucial role in regulating regional and global climate systems (Huang et al., 2017; Tan and Storelvmo, 2019; Zib et al., 2012). Understanding the properties and effects of Arctic clouds is of great importance, as they both respond to and drive climate change in this sensitive polar environment (Morrison et al., 2012; Kay et al., 2016; Taylor et al., 2022, 2023).

Despite the extreme weather and pristine conditions, several efforts have been made over time to improve the quantity and quality of observations of Arctic clouds and their radiative characteristics. A general description of the long-term Arctic stations is presented in Uttal et al. (2016). The stations mentioned in Uttal et al. (2016) have been pioneering observation sites to further investigate and explain processes and feedback mechanisms in the Arctic region related to regional processes and transport, the atmosphere, and atmosphere-surface exchanges.

Seasonal airborne and shipborne research campaigns have been crucial in collecting atmospheric and surface observations in unexplored regions with limited observations, where processes related to this rapidly changing environment remain elusive (see Table 1 in Wendisch et al. (2019)). In addition to these extensive efforts, the Multidisciplinary drifting Observatory for the Study of Arctic Climate (MOSAiC) expedition, conducted from October 2019 to September 2020 (Shupe et al., 2020), aimed to extend the collection of relevant observations related to the Arctic environment. This international collaboration of unprecedented magnitude for an Arctic research cruise provided diverse in-situ and remote sensing observations, allowing investigation of various processes related to Arctic clouds and their interactions with the Arctic system (D. and Rex, 2022).

Satellite observations have particular advantages due to their spatial coverage and long duration of service (Stubenrauch et al., 2013; Christensen et al., 2016; Huang et al., 2017). For instance, Eastman and Warren (2010) compared surface cloud observations with data sets from the Advanced Very High Resolution Radiometer (AVHRR) and Television and Infrared Observation Satellite (TIROS) Operational Vertical Sounder (TOVS). Their comparison highlighted the difficulty in finding agreement between both points of view and the additional challenges encountered during polar night, especially over icy surfaces. Additionally, Hartmann and Ceppi (2014) observed large changes in the Arctic radiation budget at the top of the atmosphere (TOA) based on CERES (Clouds and the Earth's Radiant Energy System) observations, with trends of -5 $\mathrm{W\,m^{-2}}$ and 3 $\mathrm{W\,m^{-2}}$ per decade for the shortwave and longwave net fluxes, respectively. The trend analysis focused on the Arctic boreal zone considering the CERES Energy Balanced and Filled (EBAF) data products from 2001 to 2017 and reported a decrease of the reflected solar radiation by $1.3 \pm 0.6\mathrm{W\,m^{-2}}$ per decade and an increase of the outgoing terrestrial radiation by $1.1 \pm 0.4\ \mathrm{W\,m^{-2}}$, results that suggest a greening effect of Arctic tundra that contribute to a decadal decrease of the surface albedo (Duncan et al., 2020). The study of Lelli et al. (2023) extensively analysed the regional and seasonal radiative influence of clouds on radiation based on GOME and SCIAMACHY observations over two decades. This study found that the reduction in Arctic albedo at the top of the atmosphere is compensated by the increase in atmospheric reflectivity due to a significant increase in liquid-phase clouds. More recently, Cesana et al. (2024) found a correlation between Arctic sea ice, cloud phase and radiation based on A-train satellites and CERES observations. This study found that as sea ice cover decreases, the frequency of liquid clouds is more likely to increase leading to a cooling the surface, damping the surface warming during polar day.

https://doi.org/10.5194/egusphere-2024-2193
Preprint. Discussion started: 30 July 2024

Considering satellite and ground-based inter-comparisons, the investigation by Dong et al. (2016) and Riihelä et al. (2017) compared ground- and satellite-based flux observations in a series of radiative closure studies for the ARM NSA, and the Tara drifting ice camp and observations on the Greenland Ice Sheet, respectively. Both studies considered the CERES Synoptic 1-degree daily flux (SYN1deg) product (Minnis et al., 2021), and found a good agreement based on ground radiative flux observations that were within instrumental uncertainties. The study of Barrientos-Velasco et al. (2022) investigated the effect of clouds on the radiation budget for the early summer PS106 shipborne campaign (Macke and Flores, 2018; Wendisch et al., 2019) and made a comparison between shipborne measurements and collocated satellite products and observations from CERES SYN1deg Ed.4 (hereafter denoted as CERES SYN). Barrientos-Velasco et al. (2022) found that for PS106 the solar radiation dominated the cloud radiative effect by cooling the surface by -8.8 $\mathrm{W\,m^{-2}}$ and the TOA by -48.4 $\mathrm{W\,m^{-2}}$. This analysis also evaluated cloud macro and microphysical retrievals based on active and passive shipborne remote sensing observations highlighting the frequent underestimation of cloud optical thickness and identifying additional challenges in cloud retrievals during low-level-stratus clouds (Griesche et al., 2023).

More recently, the study by Huang et al. (2022) investigated the sources of uncertainties in the Arctic surface radiation budget derived from CERES, with a particular focus on the representations of surface albedo during the MOSAiC. They found that CERES SYN1deg products underestimated the surface albedo by approximately 0.15 relative to the surface observations and underestimated the atmospheric optical thickness.

To extend the latter analysis and further exploit the capabilities of ground-based and satellite observations, in this paper, we analyse 1D radiative transfer simulations with a focus on the unprecedented yearlong international and interdisciplinary MOSAiC expedition carried out on board the research vessel (RV) *Polarstern* (D. and Rex, 2022) that collected unique observations of the ocean (Rabe et al., 2022), sea ice (Nicolaus et al., 2022), and atmosphere (Shupe et al., 2022) properties in the central Arctic. The objective of this paper is to quantify and examine the radiation budget during MOSAiC based on ship-borne and satellite-based remote sensing observations and products, and to evaluate the radiative effect of clouds during MOSAiC at the surface and the TOA. Our research questions are as follows:

1. How well can state-of-the-art cloud remote sensing retrievals and radiative transfer calculations represent the Arctic radiation budget and cloud radiative effects?
2. How does the radiation budget vary during the full annual cycle covered by the MOSAiC expedition?
3. What is the radiative effect of clouds on the radiation budget during MOSAiC?

The manuscript is subdivided into the following sections: Section 2 describes the observations and products used in this article. Section 3 details the methodology used for the analysis, followed by Section 4, which presents the results and discussions in several subsections that focus on the analysis at the surface and the TOA. Finally, the article concludes in Section 5, presenting the summary, conclusions, and outlook.

https://doi.org/10.5194/egusphere-2024-2193
Preprint. Discussion started: 30 July 2024

2 Observations and datasets

This section provides an overview of the data sources used in this study based on shipborne and ice floe observations, satellite data products, and supplementary datasets.

2.1 MOSAiC observations and datasets

Shupe et al. (2022) and Cox et al. (2023e) provide a detailed overview of the atmospheric remote sensing and in situ meteorological observations carried out on board *Polarstern* (PS) and at the MOSAiC Surface Observatory (SO), respectively. In this section, we specifically address the observations used in this study as referenced in Table 1.

2.1.1 Ship-borne instrumentation

On board *Polarstern* there was a suite of active and passive remote sensing instruments used to observe cloud and aerosol properties during MOSAiC. This instrumentation was installed at *Polarstern*'s bow at about 10 metres above sea level (see Fig. 3 in Shupe et al. (2022)). As part of the ARM Mobile Facility (Miller et al., 2016), a 35-GHz Ka-band ARM Zenith Radar (KAZR) provided information on radar reflectivity, mean Doppler velocity, and spectrum width (Johnson et al., 2014; Wang et al., 2022). A high spectral resolution lidar and a Micropulse lidar were installed providing information about the backscatter and depolarisation ratio (Morris et al., 1996; Sivaraman et al., 2019). Atmospheric liquid water path (LWP) was derived from the combination of two microwave radiometers, a two-channel sensor (Zhang, 1996) and a Microwave Radiometer for Arctic Clouds (MiRAC-P) (Ebell et al., 2022). In addition, radiosondes were launched every 6 hours from *Polarstern* to provide information about the thermodynamic and kinematic state of the atmosphere (Maturilli et al., 2021).

The synergistic combination of these instruments and radiosondes is used to characterise cloud and aerosol properties during MOSAiC. Section 3.1 summarises the methodology implemented to derive the cloud macro and microphysical properties of clouds.

2.1.2 Ice floe observations

During the MOSAiC expedition, several observations of surface and meteorological properties were measured at different locations of the SO. A 10 metre meteorological tower, a 23-30 metre mast, and a radiation station were deployed at Met-City. Three mobile Atmospheric Surface Flux Stations (ASFS), named ASFS-30, ASFS-40 and ASFS-50, were deployed in the MOSAiC distributed network, but were also used closer to *Polarstern* during some periods. The spatial coverage of these observations ranged from hundreds of metres to approximately 20 kilometres relative to the location of *Polarstern*, as shown in Fig. 3 of Cox et al. (2023e); the reasons for these changes was logistical and is explained in the referenced literature. For this study we use the Met-City and ASFS observations of skin temperature, and broadband terrestrial (Terr) and solar (Sol) upwelling and downwelling radiative fluxes. While upwelling fluxes may express local variability, the downwelling fluxes are considered regionally representative (Rabe et al., 2024).

https://doi.org/10.5194/egusphere-2024-2193
Preprint. Discussion started: 30 July 2024

The temporal coverage of surface radiation observations varied across the MOSAiC period. Observations at Met-City were made from mid-October 2019 to mid-May 2020 followed by data collection from the end of June to July 2020, after which the ice floe broke apart at the edge of the ice pack. From the end of August to mid-September 2020 Met-City observations were made again from a new ice floe farther north. ASFS-30 had the largest temporal coverage and collected data from mid-October 2019 to mid-September 2020, with a few gaps in November 2019, February 2020, May 2020, and the end of August. ASFS-40's observations were continuous from early October 2019 to the end of March 2020, while ASFS-50's observations were made from early October 2019 to mid-September 2020, but with significant data gaps between mid-January and mid-March 2020, and May 2020. The narrative is general for each station; each variable was quality controlled and some smaller gaps for several hours due to quality issues and maintenance (Cox et al., 2023e).

The upwelling and downwelling broadband solar radiative fluxes at Met-City were measured by upward-looking and downward-looking Eppley Precision Spectral Pyranometers (PSP; 0.285 - 3.0 μm), whereas the terrestrial fluxes were measured with Eppley Precision Infrared Radiometers (PIR; 3.5 - 50 μm) at 1 Hz sampling rate (see Table 1 in Cox et al. (2023e)). At ASFS stations, downward and upward-looking pyranometers were Hukseflux SR30-D1 and pyrgeometers were IR20-T2 (Cox et al., 2023e). The skin temperature provided at all four sites was derived using information from both upwelling and downwelling terrestrial observations, assuming a surface emissivity of 0.985 (see Eq. 3 in Cox et al. (2023e)). The sensor heights were approximately 2 m above the surface.

2.2 Satellite observations

This study uses the CERES SYN1deg Ed. 4 satellite products with hourly resolution (Gupta et al., 2010; Rose et al., 2013; Rutan et al., 2015; Kato et al., 2018; Minnis et al., 2021), referred to here as CERES SYN. The data includes global coverage of solar and terrestrial radiative fluxes at the top of the atmosphere and at the surface with a spatial resolution of 1° latitude by 1° longitude. Fluxes at the top-of-atmosphere are inferred from CERES radiance observations using empirical angular directional models. Fluxes within the atmosphere and at the surface are calculated using the four-stream Langley Fu-Liou radiative transfer model (Fu and Liou, 1992, 1993; Fu et al., 1998; Kratz and Rose, 1999; Kato et al., 1999, 2005), adjusting inputs to ensure consistency with the TOA fluxes. The cloud properties used in these calculations were derived from Moderate Resolution Imaging Spectroradiometer (MODIS) radiances (Minnis et al., 2021) Temporal interpolation is achieved at lower latitudes by means of geostationary satellite observations, while relying on the improved temporal sampling of polar-orbiting satellites in polar regions. The CERES SYN product also use atmospheric reanalysis data from the Global Modeling Assimilation Office Goddard Earth Observing System (GEOS-5) model version 5.4 as ancillary input (Rienecker, 2008). Furthermore, surface spectral albedo is based on lookup tables from Jin et al. (2004) and the broadband albedo is based on Terra surface albedo history maps that are consistent with clear-sky TOA albedo estimates from CERES measurements (Rutan et al., 2015).

The CERES SYN radiative fluxes are given assuming four different atmospheric conditions. The first is the all-sky (AS) condition, which takes into account both clouds and aerosols in the atmosphere. The second is the cloudless sky (CS) condition, which considers only the presence of aerosols in the atmosphere. The third is the pristine (Pr) condition, where there are no clouds or aerosols present. Finally, the fourth condition is all-sky no aerosols (NAER), where clouds are present, but no

https://doi.org/10.5194/egusphere-2024-2193
Preprint. Discussion started: 30 July 2024

aerosols are considered. The CERES SYN dataset provides radiative fluxes at the surface and at the TOA, which is defined for the calculations as 20 km.

Besides the radiative flux datasets, various surface, cloud, and aerosol parameters are included in the CERES SYN dataset. Considered in this study are cloud base pressure (P_B), cloud top pressure (P_T), cloud top temperature, cloud base temperature, cloud fraction (CF), LWP, ice water path (IWP), liquid droplet effective radius $r_{E,L}$, and ice crystal effective radius $r_{E,I}$. The CERES SYN product use the aerosol optical depth (AOD) obtained from the Model of Atmospheric Transport and Chemistry (MATCH; Collins et al. (2001)) data that assimilates retrievals from MODIS (Rutan et al., 2015).

2.3 Ancillary data

Several ancillary datasets were used as input parameters for the radiative transfer simulations and overall analysis in this article. Pressure level profiles of temperature, pressure, ozone mass mixing ratio and specific humidity from the European Centre for Medium-Range Weather Forecasts (ECMWF) Re-Analysis (ERA5) (Hersbach et al., 2020) at 1-hour resolution and 0.25 ° spatial latitudinal and longitudinal resolution. Additionally, dry-air mole fraction from the carbon dioxide, nitrous oxide, methane, chlorofluorocarbon (CFC) 11, CFC-12, and Carbon tetrachloride (CCl_4) from the NOAA Global Monitoring Laboratory's annual greenhouse gas index (AGGI; https://gml.noaa.gov/aggi/aggi.html) was used. The aforementioned radiosoundings were processed to remove in influence of *Polarstern* and blended with Met-City data to better represent near-surface meteorology, as the radiosondes were launched from the deck at approximately 20 m height (Dahlke et al., 2023).

3 Methodology

This section is divided into two parts. The first part gives an overview of the ShupeTurner cloud retrievals, and the second part addresses the methodology implemented for the radiative transfer simulations.

3.1 ShupeTurner cloud retrievals for MOSAiC

The ShupeTurner cloud retrievals provide time-resolved vertical profiles of the macro- and microphysical properties of clouds based on active and passive remote sensing observations. The retrievals were first introduced in Shupe et al. (2015) (hereafter ST2015) and applied to observations at Utqiaġvik, Alaska (71.323°N, 156.615°W), for the two-year period from March 2004 to February 2006. ST2015 describes the algorithm, including both its assumptions and uncertainties. Moreover, a comparison with the ARM Microbase cloud product (Dunn et al., 2011), as well as a closure analysis of solar and terrestrial downward fluxes have been presented.

As applied to MOSAiC, the ShupeTurner retrievals utilise cloud radar, depolarisation lidar, microwave radiometer, ceilometer, and radiosonde observations collected on board *Polarstern* as inputs (see Table 1). Reflectivities from the KAZR radar were adjusted above 3 km to statistically match the observations below 3 km due to a known calibration offset between two different radar operational modes. The low-level measurements have been determined to have the best calibration during MOSAiC. Short gaps in KAZR data were filled by a co-located W-band cloud radar, which were also calibration adjusted to match the

https://doi.org/10.5194/egusphere-2024-2193
Preprint. Discussion started: 30 July 2024

KAZR atmospheric profiles of temperature, pressure and humidity were obtained from the radiosondes. The LWP was taken from either of the two microwave radiometers to ensure maximal coverage.

Several improvements beyond ST2015 were made in the cloud phase classification (Shupe, 2007). A novel set of thresholds were developed from the cloud-free background on the Micropulse lidar depolarisation ratio signal-to-noise and total backscatter measurements using the MOSAiC data. The cloud phase was also corrected to account for lidar attenuation in the presence of liquid-containing cloud layers. For such cases, if the cloud radar observed a cloud top that is within 750 m, then the same cloud type is considered from the attenuation height up to the cloud top. In contrast to the retrievals for Utqiaġvik, Alaska, the default liquid droplet effective radius was changed from 8 $\mu\mathrm{m}$ to 9 $\mu\mathrm{m}$, which is based on aircraft measurements from the region (Shupe et al., 2005).

The ShupeTurner products provide information on cloud type phase as well as the content of liquid (LWC) and ice water (IWC). Effective radius is also calculated for liquid droplets ($r_{E,L}$) and ice crystals ($r_{E,I}$), along with the vertical integral of LWP and IWP. The dataset has a 1-minute time resolution and covers a vertical range from 160 m up to 18 km by 596 equidistant height layers, each with a thickness of 30 m.

3.2 Single column radiative transfer configuration

The radiative transfer simulations are obtained from the TROPOS Cloud and Aerosol Radiative effect Simulator (hereafter TCARS), which is a Python-based framework that carries out 1D radiative transfer simulations using the interfaces of radiative transfer models. Parts of this framework have already been applied and described in previous studies (Barlakas et al., 2020; Witthuhn et al., 2021; Barrientos-Velasco et al., 2022; Griesche et al., 2023, 2024). TCARS uses various sources of input data such as atmospheric profiles of trace gases, temperature, humidity, properties of clouds, aerosols, and surface parameters. The present study employs the widely used rapid radiative transfer model (RRTM) for GCM applications (RRTMG; Mlawer et al. (1997); Barker et al. (2003); Clough et al. (2005)). The RRTMG model operates with a Python interface version 0.9.1 detailed in Deneke (2024).

The input parameters for the radiative transfer simulation configuration are listed in Table 1. For the atmospheric profiles of temperature, pressure, humidity and ozone, we use hourly pressure level profiles from ERA5, which assimilate information from the Vaisala Radiosonde RS41 that were launched every 6 hours during MOSAiC (Hersbach et al., 2020). This dataset was selected due to its consistent temporal and spatial coverage and well-resolved atmospheric data covering up to 20 km as well as showing good similarities with radiosonde observations (Fig. B1). For trace gases, we used the uniformly distributed values of CO, CO_2, CH_4, N_2O, CCl_4, CFC-12, HCFC-22 and CFC-11, from the Annual Greenhouse Gas Index (AGGI).

The atmospheric profiles of cloud properties are based on ShupeTurner retrievals. The information added to the model is the LWC, IWC, liquid driplet effective radius ($r_{E,L}$), and ice crystal effective radius ($r_{E,I}$). The RRTMG parameterizations selected for ice and liquid cloud optical properties are based on the radiative transfer model Streamer (Key, 1996) and Hu and Stamnes (1993), respectively. The parameterization of $r_{E,L}$ in RRTMG only allows values in the range from 2.5 to 60 μm. The parameterization for ice clouds in RRTMG assumes spherical ice crystals shape to be consistent with ShupeTurner

https://doi.org/10.5194/egusphere-2024-2193
Preprint. Discussion started: 30 July 2024

assumptions (Sassen, 1987; Atlas et al., 1995; Shupe et al., 2015). In this case, RRTMG allows $r_{E,I}$ within the range between 5.0 and 131.0 μm.

Several experiments were conducted based on different sources of surface albedo datasets (see Fig. B3). First, the surface albedo from the CERES SYN product was utilised as an input parameter to calculate the radiative fluxes, denoted as TCARSe1. This dataset is interpolated in both space and time to match the position of *Polarstern* at a 1-minute resolution throughout the MOSAiC cruise. We chose to use this dataset as an input parameter since one of our objectives is to quantify flux differences related to cloud properties rather than surface differences. The comparison of ice-floe measured and surface albedo derived from CERES SYN is discussed in Huang et al. (2022).

The second and third sources of surface albedo come from the observations at ASFS-30 and ASFS-50 stations (see Fig. B3). The radiative flux calculations derived from these two sources are referred to as TCARSe2 and TCARSe3, respectively. This observed surface albedo was derived by calculating the daily mean ratio between the broadband upwelling and downwelling solar flux. Note that the rest of the input parameters for TCARSe2 and TCARSe3 remain the same as TCARSe1.

The surface emissivity is set to a constant value based on the fraction of sea ice in the vicinity of *Polarstern*, which is also obtained from CERES SYN product. When the sea ice fraction reaches or exceeds 50 $\%$, a constant surface emissivity of 0.9999 is used. If the sea ice fraction is below this threshold, a constant of 0.9907 is used instead. These constant values are based on Wilber et al. (1999). It is worth mentioning that this assumption is not the same as the one assumed for deriving the skin temperature from surface measurements (see Eq. 3 in Cox et al. (2023e)). However, we expect that this difference does not exceed by more than 1 $\mathrm{W\,m^{-2}}$ the Terr-U at the surface during cloudless conditions (see Table A2 in Barrientos-Velasco et al. (2022)).

Skin temperature is obtained from the derived product by Cox et al. (2023b) at station ASFS-30 due to its extensive temporal coverage. When this data is unavailable, skin temperature from Met-City is utilised (Cox et al., 2023a). In instances when no skin temperature data is available, but the ShupeTurner products are available, skin temperature from CERES SYN is used instead for completeness. These latter cases were rare but occurred more frequently in August 2020 (i.e., 2020-08-02 to 2020-08-20).

Several approaches for specifying skin temperature were tested, including using only ERA5 or only CERES SYN. We chose to use derived skin temperature from ice-floe observations at MOSAiC to quantify the flux differences between CERES SYN product and observations, providing a more realistic calculation of the upwelling terrestrial flux (Terr-U). Another version of the simulations using skin temperature from ERA5 is excluded in this article since this data source led to an overestimation of skin temperature, especially during Polar Night, when the largest bias was found during cloudless conditions (see Fig. C2; Herrmannsdörfer et al. (2023)).

All input parameters are linearly interpolated to a predefined standard grid, which consists of 632 atmospheric levels ranging from 40 m up to 20 km in altitude, defined as the TOA to be consistent with the definition of TOA from CERES SYN, with a temporal resolution of 1 minute. The first 600 levels of the atmosphere were divided into equidistant layers of 30 m each, and from 18.01 to 20 km, each layer was divided into 63.2 m. In total, 327, 126, and 83 TCARSe1, TCARSe2, and TCARSe3 output daily files were generated, respectively, with the temporal coverage illustrated in Fig. A1. The generated output files

https://doi.org/10.5194/egusphere-2024-2193
Preprint. Discussion started: 30 July 2024

contain vertical profiles of broadband upwelling and downwelling solar and terrestrial fluxes, and heating rates for both cloudy and cloudless conditions during the MOSAiC period.

This study follows the definition by Rossow and Zhang (1995) and Mace et al. (2006) of the cloud radiative effect (CRE) as the difference in radiation between a cloudy and an atmosphere without clouds at the surface and the TOA. In this article, we discuss two calculation methods: one based on the difference between simulated all-sky conditions minus simulated cloudless conditions, and another term named "hybrid", which subtracts the observed radiative flux from the cloudless simulations. This difference is measured in units of $\mathrm{W\,m^{-2}}$. The Net CRE is calculated by adding the Terr CRE and Sol CRE components, which are calculated using Equation (1). In this equation, "x" represents either terrestrial or solar radiation and is calculated at both the surface and the TOA. The atmospheric CRE is defined as the difference between the TOA and the surface. This terminology and methodology are based on previous research by Barrientos-Velasco et al. (2022). A positive value indicates warming, while a negative value indicates cooling due to the presence of clouds.

$$CRE_x = (F_x^{\downarrow} - F_x^{\uparrow})_{All-sky} - (F_x^{\downarrow} - F_x^{\uparrow})_{Cloudless}. \quad (1)$$

4 Results and discussions

In this section, we provide a general overview of the atmospheric and surface conditions during MOSAiC. We perform a detailed radiative closure analysis to understand flux biases, followed by an evaluation of the net longwave radiation to infer the atmospheric opacity. The last subsection presents the quantification of the radiation budget using ship-borne and satellite remote sensing observations and products, followed by the investigation of the radiative effect of clouds.

4.1 General overview of atmospheric and surface conditions

The RV *Polarstern* drifted with the Arctic sea ice from the Laptev Sea to the Fram Strait, crossing through the central Arctic region from October 2019 to September 2020. For our analysis, we divided the time series into four periods: two during the Polar Night (from October 15, 2019, to March 13, 2020) and two during the Polar Day (from March 14, 2020, to September 20, 2020) to characterise seasonal differences (Fig. 1). Additionally, we consider the entire MOSAiC period from October 15, 2019, to September 20, 2020.

The second half of October 2019 was characterised by almost average near-surface meteorological conditions with 2-m air temperature decreasing from about 263 to 255 K (Rinke et al., 2021). This period was characterised by a high frequency of single-layer clouds (see Fig. 2a) and a high frequency of occurrence of low-level jets (López-García et al., 2022) that potentially were a source of turbulence into the atmospheric boundary layer contributing to a weakly stable atmospheric regime (Jozef et al., 2023). The first storms were observed over the MOSAiC location in November. November 16-20 was characterised by high winds and moist air from the North Atlantic that caused leads to form and periodic power outages at the SO that broke the continuity of measurements (Nicolaus et al., 2022; Cox et al., 2023e). The lead formation event in mid-November coincides with an intermittent decrease of sea ice thickness (Krumpen et al., 2021). The steady increase of integrated water vapour was

https://doi.org/10.5194/egusphere-2024-2193
Preprint. Discussion started: 30 July 2024

from 2 to 8 $\mathrm{kg\,m^{-2}}$ (Heinemann et al., 2023), values that are considered record-breaking in comparison to the climatology (Rinke et al., 2021).

During MOSAiC, the coldest atmospheric conditions were observed from December to mid-March (Herrmannsdörfer et al., 2023). The 2-m air temperature decreased as low as about 231 K, which was the coldest temperature recorded. The stratospheric temperature also dropped below 200 K (Fig. C1). However, there were two exceptions to this pattern. In early December (December 3-5) and in February (February 18-22), warm air-mass intrusions (WAI) originating from Siberia reached MOSAiC, causing a temporary increase in temperature (Herrmannsdörfer et al., 2023; Rinke et al., 2021). Contrary to the WAI, a marine cold-air outbreak (MCAO) was identified in March with the centre over the Fram Strait region and linked to northerly winds (Rinke et al., 2021; Murray-Watson et al., 2023). From January to March 2020 a record-breaking positive phase of the Arctic Oscillation (AO) index was observed indicating that the low-pressure anomaly in the Arctic was surrounded by a ring of high pressure at mid-latitudes that potentially facilitated the transport of mid-latitude air masses (Lawrence et al., 2020; Rinke et al., 2021; Boyer et al., 2023).

April 2020 was characterised by two WAIs that led to an anomalous increase of near-surface air temperature from 242.4 to 270.0 K from April 14 to April 21 (Shupe et al., 2022). The analysis of Kirbus et al. (2023) suggested that this WAI was associated with a Siberian and Atlantic pattern that led to a strong positive effect on the surface energy budget dominated by turbulent heat fluxes over the ocean and strong radiative influence over sea ice. The increase in temperature during this event was associated with the increase in the concentration of water vapour with values that exceeded 10 $\mathrm{kg\,m^{-2}}$ (Kirbus et al., 2023). This unprecedented increase in temperature led to several changes in conditions in the atmosphere (Dada et al., 2022; Svensson et al., 2023) and at the surface (Krumpen et al., 2021; Rückert et al., 2023). This period was also used as a first example of the improvement in how nudging a large-scale circulation model to observations improved and accelerated the model evaluation (Pithan et al., 2023).

May was characterised by anomalously warm temperatures that were more prominent during the second half of the month (Rinke et al., 2021). From mid-May to June *Polarstern* left the MOSAiC SO for an exchange of personnel at the fjord of Svalbard (D. and Rex, 2022). The months of July and August were considered the warmest for the 1979 to 2020 period. The atmospheric conditions during this period were moister than the climatological values with values of total column water vapour up to 30 $\mathrm{kg\,m^{-2}}$ (Rinke et al., 2021). In July 2020, a large decrease of surface albedo was observed, led by an increase of pond fraction by 20 % (Webster et al., 2022), especially between July 11 and 13 when melt-pond drainage was observed (Webster et al., 2022; Light et al., 2022).

Finally, in September 2020, the near-surface temperatures started to decrease to temperatures below 273.15 K allowing ice-floe ponds to freeze up (Webster et al., 2022; Light et al., 2022). Despite the expected decrease of temperature and moisture in the atmosphere for this time of year, two WAI were observed in the middle of September that were associated with an increase in humidity, temperature and heat transport from lower latitudes (Rinke et al., 2021).

https://doi.org/10.5194/egusphere-2024-2193
Preprint. Discussion started: 30 July 2024

4.2 Consistency of cloudless simulations

One of our objectives is to compare surface radiative fluxes from atmospheric radiative transfer simulations based on MOSAiC observations to fluxes from the CERES SYN product. To test the consistency between CERES SYN and TCARS simulations, we first compared the calculated fluxes for cloudless simulations.

In this section, we will focus on the TCARSe1 cloudless simulations (see Section 3.2, Fig. A1). The TCARSe1 simulations and CERES SYN product rely on different data sources for atmospheric and surface conditions, such as skin temperature and atmospheric profiles of humidity and temperature. They also use different radiative transfer models. Therefore, prior to conducting the all-sky radiative closure assessment for the MOSAiC period, it is necessary to understand the differences between both fluxes under cloudless conditions.

This analysis focuses on all available TCARSe1 simulations from 2019-10-15 to 2020-09-20 and CERES SYN collocated products to the location of *Polarstern*. To illustrate the cloudless flux comparison between both datasets, a series of comparative plots are shown in Appendix C.

The comparison of Terr-D at the surface between TCARSe1 and CERES SYN shows an agreement with correlations larger than 0.9 and biases no larger than 9.6 $\mathrm{W\,m^{-2}}$ (see Fig. C1). The largest discrepancies are from 2019-10-16 to 2019-10-19 and between 2019-11-11 to 2019-11-22 when the TCARSe1 flux surpasses CERES SYN leading to average flux differences of 25.2 $\mathrm{W\,m^{-2}}$ and 32.3 $\mathrm{W\,m^{-2}}$, respectively. The November period coincided with the WAI described in Section 4.1 (Heinemann et al., 2023). While during this period the cloud occurrence was high, the few cloudless periods identified (i.e., 2019-11-13 6:30Z-22:00Z) indicate a good agreement between the TCARSe1 simulations and observations at the ASFS-40 station with a mean (maximum) flux difference of 1.8 $\mathrm{W\,m^{-2}}$ (5.3 $\mathrm{W\,m^{-2}}$).

During the spring, in contrast to Polar night months, CERES SYN product show larger Terr-D values than TCARSe1 results (see Fig. C1c). The mean flux difference between both datasets for the period 2020-03-14 to 2020-05-31 is 3.5 $\mathrm{W\,m^{-2}}$ and shows the best correlation of 0.98. From June 9, 2020, until the end of MOSAiC, the TCARSe1 cloudless Terr-D fluxes are larger than CERES SYN values as during the 2019-10-15 to 2019-12-31 period (Fig. C1b), but with a smaller magnitude.

The last period with the largest Terr-D flux discrepancies was observed between 2020-08-01 and 2020-08-21, with a mean flux difference of 13.2 $\mathrm{W\,m^{-2}}$. Unfortunately, during this period, no observations at MOSAiC SO were collected; thus, no additional comparison with ice-floe observations could be made to determine which dataset was closer to the observations under cloudless conditions.

The comparison of cloudless Terr-U flux at the surface indicated a consistent agreement between both datasets with biases below 5.9 $\mathrm{W\,m^{-2}}$ and correlations larger than 0.87 (see Fig. C2). The comparison of skin temperature in Fig. B2 shows a relatively good agreement between CERES SYN and the MOSAiC SO observations for all months except September 2020, where CERES SYN values are notably lower than the observations. The largest difference occurs between 2020-09-14 to 2020-09-20 when the mean and maximum flux difference is 21.6 and 27.5 $\mathrm{W\,m^{-2}}$, respectively. This period coincides with two storms with WAI events that brought moisture leading to rain on snow, events described earlier and reported in Rinke et al. (2021) and Shupe et al. (2022).

https://doi.org/10.5194/egusphere-2024-2193
Preprint. Discussion started: 30 July 2024

It is noteworthy that the Kernell Density Estimate (KDE) distribution of the cloudless Terr-U flux difference for the period 2019-10-15 to 2019-12-31 shows a bi-modal distribution (see Fig. C2a). Two sub-periods explain the distribution around 18 $\mathrm{W\,m^{-2}}$. The periods between 2019-10-28 to 2019-11-09, and from 2020-12-15 to 2019-12-25 show a mean cloudless Terr-U flux difference of 11.0 $\mathrm{W\,m^{-2}}$ and 10.9 $\mathrm{W\,m^{-2}}$, respectively, with the highest differences up to 35.7 $\mathrm{W\,m^{-2}}$ as observed for December 21 and 22. Both periods coincide with anomalously cold periods that are lower than the median over 1979-2019 (see Fig. 1 in Rinke et al. (2021)).

The cloudless comparison of Sol-D is illustrated in Fig. C3a, b, e, and f. While the correlation coefficient for the comparison is near 1.0, the distributions reveal an unimodal distribution centred near zero for both cloudless and pristine conditions (depicted in green). The mean flux differences for the period between 2020-03-14 and 2020-05-31 are 2.9 $\mathrm{W\,m^{-2}}$ for cloudless conditions and -3.1 $\mathrm{W\,m^{-2}}$ for pristine conditions.

For the period between 2020-06-01 and 2020-09-20, the comparison indicates consistent good agreement between TCARSe1 simulations and CERES SYN pristine products. The comparison between CERES SYN cloudless and CERES pristine products suggests that the presence of aerosols reduces Sol-D by about 6.0 $\mathrm{W\,m^{-2}}$ during the first Polar day period and by 15.3 $\mathrm{W\,m^{-2}}$ during the second Polar day period.

As all versions of TCARS simulations do not account for the presence of aerosols in the atmosphere, given that the main focus was on the influence of clouds on the radiation budget, these differences due to the presence of aerosols are nonetheless considered in the analysis presented in the following sections.

The mean Sol-U flux difference between TCARSe1 simulated fluxes and CERES SYN product at the SFC is 2.4 $\mathrm{W\,m^{-2}}$ for the first Polar day period (Fig. C3c) and 7.2 $\mathrm{W\,m^{-2}}$ for the second Polar day period (Fig. C3d). The comparison between TCARSe1 and CERES SYN pristine products shows biases of -2.6 $\mathrm{W\,m^{-2}}$ and -2.0 $\mathrm{W\,m^{-2}}$ for the respective Polar day periods. Differences arise since the presence of aerosols reduces the amount of solar radiation reaching the surface, thereby decreasing its availability to be reflected. Consequently, the similarity in KDE distributions of Sol-D and Sol-U fluxes reflects the dependence of both components on the radiative transfer calculations.

At the TOA, the cloudless Terr-U and Sol-U fluxes exhibit good agreement between TCARSe1 simulations and CERES SYN product. All correlation coefficients are higher than 0.89, and the distributions are centred around zero. The mean flux differences are below $\pm$4.5 $\mathrm{W\,m^{-2}}$ within the instrumental uncertainty and consistent between both datasets (see Fig. C4 and Fig. C5).

In general, the cloudless comparison between TCARSe1 simulations and CERES SYN product suggests a reliable comparison. Nevertheless, it is important to consider the periods during which the disagreement is more significant due to an underestimation of temperature and humidity from CERES SYN leading to an underestimation of the Terr-D flux and the omitted direct influence of aerosols under cloudless conditions reducing the Sol-D flux for TCARS simulations.

4.3 Radiative closure assessment

The three versions of TCARS simulations and CERES SYN product are evaluated within the context of a radiative closure analysis that is defined as acceptable if the biases are within the assessed uncertainty of the measurements. To be consistent

https://doi.org/10.5194/egusphere-2024-2193
Preprint. Discussion started: 30 July 2024

with previous studies (i.e., Dong et al. (2016); Ebell et al. (2020); Barrientos-Velasco et al. (2022)) we consider acceptable biases no larger than $\pm 10.0\ \mathrm{W\,m^{-2}}$ for the Terr-D and $\pm 20.0\ \mathrm{W\,m^{-2}}$ for the Sol-D as these values are considered to be the maximum uncertainty in polar regions (Lanconelli et al., 2011). The global annual mean net surface flux uncertainty for CERES SYN product are within $\pm 12.0\ \mathrm{W\,m^{-2}}$, however, larger uncertainties are expected in the polar regions, especially on the upward solar flux (Kato et al., 2012).

The following radiative transfer closure assessment focuses on comparing the simulated terrestrial and solar fluxes with the observed fluxes at the surface and TOA. At the surface, the radiative closure is considered only for downwelling fluxes, while at the TOA, it is considered for upwelling fluxes. The counterparts are not evaluated as they are less dependent on clouds and the simulations use them as inputs, such as skin temperature (e.g., TCARSe1, TCARSe2, TCARSe3) and surface albedo (e.g., TCARSe2, TCARSe3). Moreover, we aim to be consistent with the methodology presented in ST2015.

Additionally, we categorise the comparison by atmospheric conditions into four main categories: All-sky, Cloudy, Cloudless, and Broken Cloud conditions, as classified by ShupeTurner. Broken Cloud conditions were derived from the cloudless screening and were identified in instances where the standard deviation among downwelling flux observations from stations exceeded $10.0\ \mathrm{W\,m^{-2}}$ during periods when more than one downwelling pyranometer or pyrgeometer was available. Including the category of Broken Cloud conditions in the analysis aims to remove any cloud contamination in the cloudless analysis. Achieving a good representation of cloudless conditions is the first step in validating the radiative transfer simulations and separating cases that are outside the scientific objectives of the current study. Our analysis does not further investigate the similarities or discrepancies of cloud phase between ShupeTurner retrievals and CERES SYN product.

The comparison includes all available high-quality ice-floe observations from ASFS stations and at Met-City, while excluding periods with rain. Rainy conditions introduce interference, either by disrupting the microwave radiometer measurements (Cadeddu et al., 2017) or obstructing the view of upward-looking pyranometers and pyrgeometers.

This section is divided into two parts. The first subsection presents a comparison between simulated and observed downwelling terrestrial and solar fluxes at the surface, and the second section compares the upwelling terrestrial and solar fluxes at the TOA.

4.3.1 Analysis at the surface

The hourly comparison between Terr-D simulated fluxes and observations at ASFS-30 shows very good agreement for TCARSe1 results, with median differences below $\pm 5\ \mathrm{W\,m^{-2}}$ for all-sky, cloudy, and cloudless atmospheric conditions (Fig. 4a, 4b, 4c, Table 2). The comparison with CERES SYN also indicates very good agreement for these conditions. However, larger differences are found for the defined cloudless atmosphere, with a median difference of $6.5\ \mathrm{W\,m^{-2}}$ (Table 2). A deeper analysis during this atmospheric condition using CERES SYN cloudless products instead of all-sky products suggests that while cloudless conditions are identified at *Polarstern*, other clouds were present within the spatial resolution of CERES SYN, reducing the biases from $13.2\ \mathrm{W\,m^{-2}}$ to -9.9 $\mathrm{W\,m^{-2}}$ (see values in parenthesis in Table 2). For both datasets, TCARSe1 and CERES SYN, the simulated Terr-D flux for cloudless conditions shows negative biases that are compensated by the presence of clouds.

https://doi.org/10.5194/egusphere-2024-2193
Preprint. Discussion started: 30 July 2024

Due to the limitations of the 1D experimental radiative transfer setup from TCARS and CERES SYN, larger biases can be expected under broken cloud conditions, which occurred about 0.6 % of the time (Fig. 4d, 4h, 4l, 4p).

The overall hourly TCARSe1 Terr-D flux comparison among all stations indicated a good agreement, suggesting that, in general, the Terr-D flux is similar despite the distances separating each station (Fig. D1a). This finding aligns with Rabe et al. (2024), which reported that in transient conditions, the temporal variability of the Terr-D was larger than the spatial variability. The spatial comparison of the collocated CERES SYN product with each station suggests that the mean flux difference is relatively dependent on the location of the observations. According to CERES SYN, the atmospheric conditions might have varied to some extent relative to the location of *Polarstern* (Fig. D2a).

The KDE distribution comparing the Sol-D flux difference between simulations and observations is illustrated in the second and forth column in Fig. C5 for TCARSe2 and CERES SYN, respectively, and the summary of the biases including all the simulations is shown in Table 3. The lowest biases found are for TCARSe2 with mean and median flux differences below $\pm 4.1\ \mathrm{W\,m^{-2}}$ for all-sky and cloudy conditions. The largest biases are found for cloudless conditions for all the simulations, but within the uncertainty threshold of $\pm 20\ \mathrm{W\,m^{-2}}$. In general, the radiative closure can be confirmed for TCARS simulations and CERES SYN.

The Sol-D flux comparison between TCARSe1 and TCARSe2 directly shows the effect that surface albedo has on radiative transfer calculations. Both TCARSe1 and TCARSe2 use the same cloud properties, but the change in surface albedo causes a mean flux difference of about $10\ \mathrm{W\,m^{-2}}$ in the Sol-D flux (Table 3). This suggests that a lower surface albedo (i.e., CERES SYN) absorbs more solar radiation at the surface, reducing the reflected solar flux from the surface to the cloud, and thus further decreasing the reflection from the cloud back to the surface. Note that the viewing differences between ground-based and satellite sensors are another factor leading to the flux differences as the ground-based observations cover an area of a few meters. In contrast, the satellite perspective has a viewing area with multiple ice floes and an open ocean. Since the ground measurements are used for the comparisons here, it is not surprising that the TCARSe2 and TCARSe3 datasets would show closer agreement.

In the study of Huang et al. (2022), several perturbation experiments were conducted varying the surface albedo and the cloud fraction. This study found that by increasing the surface albedo and the cloud fraction, the biases in the solar and terrestrial fluxes reduced, stating that the surface albedo and atmospheric opacity within the CERES SYN product are underestimated. Our results corroborate their findings, but what we find counter-intuitive is that in general the values of LWP and IWP are larger for CERES SYN than for ShupeTurner (Fig. 3). The latter might suggest that the cloud parameterizations or set up used when calculating the radiative fluxes vary in a large magnitude between the radiative transfer solver RRTMG and the four-stream Langley Fu-Liou radiative transfer model. While it is outside the scope of this study to investigate model differences, it is reported that the differences between both models are within the uncertainties set by this study (Gu, 2019).

The analysis of the Sol-D flux utilises observations from ASFS-30 and ASFS-50 (Fig. D1b, Fig. D2b). No observations were available from ASFS-40 during Polar Day, and measurements from Met-City are excluded due to a systematic error that caused lower Sol-D values for optically thin atmospheres (e.g., cloudless skies or thin ice clouds). The mean Sol-D flux difference between Met-City and ASFS-50 observations varied by approximately $18\ \mathrm{W\,m^{-2}}$ under these conditions. The underestimation

https://doi.org/10.5194/egusphere-2024-2193
Preprint. Discussion started: 30 July 2024

of Sol-D observed at Met-City during these conditions may be attributable to the instrumental characteristics of the pyranometer at Met-City (i.e., Eppley PSP), which is sensitive to incident viewing angles. More details and implications of this sensitivity for surface-based radiometric reference data sets over the global oceans is discussed in Riihimaki et al. (2024).

The ShupeTurner cloud retrievals were evaluated previously in ST2015 considering two-year atmospheric observations at Utqiaġvik, Alaska. The radiative closure assessment in ST2015 focused on the downwelling fluxes at the surface and upwelling fluxes at the TOA. The results discussed here are similar to the results reported in ST2015. The largest median flux difference is for cloudless Sol-D flux with median flux values of -15.6 $\mathrm{W\,m^{-2}}$ whereas in this study the median flux difference is 3.3 $\mathrm{W\,m^{-2}}$ (Table 3). The Sol-D flux difference in ST2015 might be due to broken cloud conditions that possibly were not excluded from their analysis. Note that the results presented in ST2015 were 10-min averages, whereas here the results are hourly averages.

The analysis of ST2015 further investigated the radiative closure assessment by sub-classifying the cloud phase of single-layer clouds into liquid, ice, and mixed-phase. Doing a similar analysis, TCARSe1 results indicate a very good agreement for Terr-D flux at the surface for the three thermodynamic conditions (i.e., liquid, ice, and mixed-phase clouds) with hourly median flux differences below $\pm$4.1 $\mathrm{W\,m^{-2}}$ (Table A2).

The results for the Sol-D flux comparison considering the three versions of TCARS simulations are shown in Table A3. At the SFC, the best agreements are found for TCARSe2 and TCARSe3, with median flux differences below $\pm$6.6 $\mathrm{W\,m^{-2}}$. When looking at the mean biases, liquid clouds show the best agreement. For ice clouds, there is a positive bias for TCARS of about 20 $\mathrm{W\,m^{-2}}$, suggesting an overestimation in cloud opacity, and in mixed-phase clouds, there is a negative bias of 8.4 $\mathrm{W\,m^{-2}}$. The effect of different surface albedo between TCARSe1 and TCARSe2 in single-layer liquid and mixed-phase clouds leads to a mean flux difference of about 12.4 $\mathrm{W\,m^{-2}}$, suggesting that with a lower surface albedo, less solar radiation is available for multiple reflections between cloud and surface. The same effect is observed for ice clouds, but to a lesser extent (4.1 $\mathrm{W\,m^{-2}}$), as they absorb Sol-D less effectively.

It is important to note that these results are subject to sample availability and hourly averaging. Increasing the time resolution of the analysis could highlight the influence of advection on observations, thereby enhancing the spatiotemporal variability of the radiative fluxes (Barrientos Velasco et al., 2018; Rabe et al., 2024). Additional analysis on how surface albedo affects the derivation of atmospheric fluxes is recommended for future studies. Improving or refining this parameter is beyond the scope of the current analysis.

4.3.2 Analysis at the top of the atmosphere

The comparison of the upwelling TCARS radiative fluxes and CERES SYN product at the TOA are illustrated in Fig. 5, Fig. D3 and reported in Tables 4 and 5. The comparison shows the difference between TCARS simulations and the collocated CERES SYN product at the locations of all the stations at MOSAiC SO. Besides evaluating the TCARS simulations at the TOA, we aim to analyse how the spatial coverage influenced the flux differences.

While the mean Terr-U flux differences are similar across all stations, ranging from -4.4 to -0.4$\mathrm{W\,m^{-2}}$, the KDE distribution indicates the best agreement at Met-City. For ASFS-30 and ASFS-50, higher distributions are observed for positive values, whereas ASFS-40 shows a higher occurrence of negative values (see the first column in Fig. 5). Despite these differences in

https://doi.org/10.5194/egusphere-2024-2193
Preprint. Discussion started: 30 July 2024

distribution, the values suggest consistency among TCARSe1 simulations, indicating a limited influence of spatial variability (Fig. D3a). Analysis of single-layer liquid, ice, and mixed-phase clouds shows biases lower than 7.5 $\mathrm{W\,m^{-2}}$, confirming the consistency of Terr-U flux in the TCARS results at the TOA (Table A2).

The comparison of the Sol-U flux comprises all the versions of TCARS simulations. Given that the surface albedo observed at MOSAiC SO is higher than CERES SYN (see Fig. B3, (Huang et al., 2022)), larger Sol-U fluxes are calculated at the TOA for TCARSe2 and TCARSe3 (Table 5). The median Sol-U flux difference is lower in magnitude than the results reported in ST2015 with values ranging between 17.4 and 21 $\mathrm{W\,m^{-2}}$ for all-sky and cloudy conditions and monomodal distributions around 0.0 $\mathrm{W\,m^{-2}}$ (see Fig. 5 second column).

The change in surface albedo affects the calculated Sol-U fluxes by 15.4 $\mathrm{W\,m^{-2}}$ during all-sky conditions and up to 25.0 $\mathrm{W\,m^{-2}}$ during cloudless conditions. The results in ST2015 are relatively similar to the ones calculated here for the Terr-U, but the comparison of Sol-U in ST2015 shows larger median flux differences ranging from -41.3 to -14.4 $\mathrm{W\,m^{-2}}$. It is worth noting that the median flux difference for cloudless conditions in ST2015 is -43.1 $\mathrm{W\,m^{-2}}$, a considerably larger value that could have been caused by differences in spatial inhomogeneities of surface properties within the satellite spatial resolution in contrast to the single column radiative transfer calculation in ST2015.

The overall TCARS terrestrial and solar upwelling flux comparison indicates a reasonably consistent agreement with CERES SYN product at the TOA supporting the use of TCARS results to be reliable to calculate the radiation budget and extend the analysis of cloud radiative effects during MOSAiC. Moreover, the differences in radiative closure highlight the important role that surface albedo, and its spatial scaling, play in comparing different products.

4.4 Evaluation of net terrestrial radiative flux

In this section, we consider the analysis of the net terrestrial radiative flux to describe the atmospheric opacity for a non-scattering atmosphere in the terrestrial spectral range. Atmospheric opacity refers to the absorption of solar and terrestrial radiation. A transparent atmosphere is one where no significant solar or terrestrial radiation is absorbed within it. Conversely, an opaque atmosphere absorbs a considerable amount of radiation, while a semi-transparent atmosphere absorbs radiation to a lesser extent than in opaque conditions (Guzman et al., 2017).

We analyse atmospheric opacity by examining variations in the net terrestrial flux (Terr-N; defined as Terr-D minus Terr-U), as this variable is related to atmospheric opacity in the terrestrial spectral range. Analysing the distribution of Terr-N aids in the interpretation and representation of atmospheric conditions in the TCARS and CERES SYN simulations. Additionally, this parameter spans the entire MOSAiC period, enabling a comprehensive understanding of the monthly atmospheric state.

The analysis of the Terr-N is based on TCARSe1 due to the good temporal coverage. Note that the analysis using TCARSe2 and TCARSe3 simulations was not made, as the analysis would lead the similar results since the only difference among the three sets of experiments is the surface albedo, and this parameter does not influence the Terr flux. Figure 6 shows the Terr-N monthly distribution for TCARSe1. The overall comparison for the entire MOSAiC period is shown in Fig. 6a. The remaining panels provide the distribution for each month. Each distribution is subdivided into two zones. Values greater than -25 $\mathrm{W\,m^{-2}}$ represent an optically thick atmosphere, and values less than - 25 $\mathrm{W\,m^{-2}}$ are defined as a semi-transparent atmosphere. Other

https://doi.org/10.5194/egusphere-2024-2193
Preprint. Discussion started: 30 July 2024

thresholds were used in other studies, where a semi-transparent atmosphere is defined from -25 to - 15 $\mathrm{W\,m^{-2}}$, cloudy atmosphere is defined for values greater than - 15 $\mathrm{W\,m^{-2}}$ and clear-sky for Terr-N fluxes lower than - 25 $\mathrm{W\,m^{-2}}$ (e.g., Solomon et al. (2023)). However, here we opted for a threshold that could also be implemented during Polar day as the values of Terr-D and Terr-U are higher.

Each panel in Fig. 6 shows the KDE distribution observed at ASFS-30 (gray), calculated from TCARSe1 (red), and CERES SYN (blue). Additionally, for October and November 2019, the distribution from ASFS-40 (green) is included and for March and April 2020 the observations at Met-City are added (orange). The observations at these stations were added as the observations had more hourly data samples compared to observations at ASFS-30. The comparison of TCARSe1 and CERES SYN product was limited to the data availability of the observations, meaning that if there were any data gaps, the exact hourly sample was removed from TCARSe1 and CERES SYN datasets for a fair comparison. For October and November 2019, the data limitation was based on ASFS-40 observations and for March and April, the datasets were limited to the data availability at Met-City. The rest of the months were limited to the observations at ASFS-30.

Based on the Terr-N comparison for the entire MOSAiC period, the atmosphere was characterised by a clear bimodal distribution in all seasons, indicating distinct occurrences of optically opaque and optically thin atmospheres. However, for the months of May through September there is a particularly frequent occurrence of optically thick atmospheres, consistent with the frequent occurrence of clouds with high LWP in these months (Fig 3a). In October 2019, the last 15 days of the month were analysed, and in September 2020, the first 20 days were evaluated showing relatively similar distributions.

The TCARSe1 Terr-N distribution generally captures the bimodal distribution observed for most months, although discrepancies arise during certain Polar Night months (e.g., November and December 2019, and January, February, and March 2020), where it tends to overestimate the occurrence of the highest opacity cases and underestimate the occurrence of low opacity cases compared to observations.

The CERES SYN Terr-N distributions exhibit considerable discrepancies with both the observed data and TCARSe1 simulations, particularly in the shapes of the KDE distributions, which generally indicate optically thinner atmospheres, as discussed in Section 4.3.1 and previously noted in Huang et al. (2022). The more negative Terr-N values are especially pronounced during Polar Night. In contrast, during Polar Day, the distributions show a better correspondence with observations. This finding aligns with Fig. 2, which highlights that the months with the largest discrepancies correspond to periods where the frequency of cloud fraction is lower than the ShupeTurner retrievals.

In February 2020, the CERES SYN Terr-N KDE distribution indicated a more frequent occurrence of semi-transparent atmospheres, leading to an overestimation of cloudless conditions and an underestimation of atmospheric opacity. A detailed analysis of several cases in this month and during September indicated a more frequent underestimation when the cloud base was misidentified during snow precipitation events identified by ShupeTurner (not shown).

September 2020 poses a particularly challenging comparison, as the Terr-N discrepancy stems not only from an underestimation of cloud opacity but also from a significant underestimation of skin temperature, leading to an underestimation of Terr-U flux values in CERES SYN product (see Fig. B2). A comparison using observed Terr-U fluxes at ASFS-30 instead of Terr-U fluxes from CERES SYN indicates a higher distribution toward a more semi-transparent atmosphere (not shown),

https://doi.org/10.5194/egusphere-2024-2193
Preprint. Discussion started: 30 July 2024

making September 2020 the period with the most pronounced underestimation of cloud opacity by CERES SYN. It is worth clarifying that from September 4 to 19, ASFS-30 was positioned over a re-freezing melt pond (Cox et al., 2023e), which may also explain these differences.

4.5 Radiation budget and cloud radiative effect (CRE) during MOSAiC

The radiation budget and the CRE are calculated for the MOSAiC period at the surface and at the TOA, utilising TCARS, CERES SYN datasets, and MOSAiC observations. This section provides both monthly and full-year statistics.

The following box plot time series presented in this section examines the TCARSe1 dataset for terrestrial flux, as these simulations cover the entire MOSAiC period. In contrast, the analysis of solar flux illustrated in the box plots uses the TCARSe2 simulations, as this dataset is based on observed daily mean surface albedo from ASFS-30 and they have a longer temporal coverage than TCARSe3 (see Section 3.2, Fig. A1). The calculation of total fluxes (i.e., Terr-N plus Sol-N) is based on the aforementioned datasets. The statistical analysis of observed terrestrial fluxes is primarily based on observations from ASFS-30, except for October 2019, when data from Met-City was used due to data availability. For completeness, we included the calculations of the radiation budget and the CRE based on TCARSe1, and TCARSe3 simulations and reduced the CERES SYN values to the data availability of TCARSe2 simulations for comparison purposes (see Table 6).

Figure 7 shows the terrestrial net (Terr-N, panel a), solar net (Sol-N, panel c), and Net fluxes (panel e) at the surface in monthly box plots. The results for each month are shown for TCARS (in red), CERES SYN (blue) and observations (black). Each month considers the same data points to illustrate a fair comparison among the datasets. The result for the entire MOSAiC period is illustrated in panels b, d and f for the Terr-N, Sol-N, and Total surface flux, respectively.

The Terr-N flux showed large variability with values ranging from around -100 $\mathrm{W\,m^{-2}}$ to positive values around 25 $\mathrm{W\,m^{-2}}$ with lower variability during July and August when the Terr-D and Terr-U at the SFC are relatively similar because of generally high cloud fraction (Fig. 2, Fig. 6k and 6i, Fig. 7a).

The variation of the upwelling and downwelling Terr fluxes at the SFC is comparable to other sites in the Arctic, as reported in Dong et al. (2010), where the climatological analysis of 10 years of observations at the ARM NSA site and NOAA Barrow Observatory in Utqiaġvik, Alaska, suggests an annual Terr-D (Terr-U) of 240.0 and 241.1 $\mathrm{W\,m^{-2}}$ (271.3 and 273.1 $\mathrm{W\,m^{-2}}$), respectively (see Fig. 2 in Dong et al. (2010)). In this study, the mean Terr-D for TCARSe2, CERES SYN and MOSAiC observations are 230.2, 224.0 and 226.5 $\mathrm{W\,m^{-2}}$, correspondingly (not shown). The mean Terr-U for TCARSe2, CERES SYN and MOSAiC observations are 251.0, 250.7, and 250.2 $\mathrm{W\,m^{-2}}$, respectively, leading to a Terr-N at the SFC of -20.8, -26.7 and -23.7 $\mathrm{W\,m^{-2}}$ for TCARSe1, CERES SYN and ASFS-30, respectively (Table 6).

The study by Ebell et al. (2020) also presents observations of downwelling terrestrial radiation (Terr-D) from June 2016 to August 2018 for Ny-Ålesund, Svalbard (see Fig. 2 in Ebell et al. (2020)). While the highest values are similarly observed in July and August, consistent with the findings here and in Dong et al. (2010), the minimum Terr-D observed during the Polar Night did not fall below 200 $\mathrm{W\,m^{-2}}$. This contrasts with the findings of this study and Dong et al. (2010), where minimum values reached around 170 $\mathrm{W\,m^{-2}}$. The higher values observed at Ny-Ålesund are characteristic of the region, as the location of the AWIPEV (Alfred Wegener Institute for Polar and Marine Research) Research Base, where the observations were collected, is

https://doi.org/10.5194/egusphere-2024-2193
Preprint. Discussion started: 30 July 2024

known for frequent atmospheric advection that transports warm and moist air, unlike other regions in the Arctic (Dahlke and Maturilli, 2017).

The solar flux at the SFC is shown in Figures 7c and 7b. The box plots for TCARSe2 and ASFS-30 exhibit relatively similar patterns across all months. In contrast, the CERES SYN data shows a clear overestimation of the Sol-N flux, primarily due to lower surface albedo values considered in CERES SYN. With an underestimation of surface albedo by -21.01 % (Huang et al., 2022), the even higher solar flux suggests an underestimation of atmospheric opacity, as more radiation is absorbed by the surface based on CERES SYN product. However, it is important to note that the underestimation of cloud opacity is more pronounced during Polar night than during Polar day months (Fig. 6). The Sol-N values for TCARSe2, CERES SYN, and ASFS-30 are 50.2, 74.3, and 46.9 $\mathrm{W\,m^{-2}}$, respectively, indicating that TCARSe2 provides a better representation of the observed Sol-N flux than the CERES SYN products (Table 6).

The Total flux at the SFC, shows a consistent dominance of the Terr flux for most of the year through March 2020 (Fig. 7e). April is the transition month where the values start to become relatively more positive. From May to August 2020 the Net fluxes at the SFC are dominated by the Sol fluxes. The first 20 days of September 2020, are also part of a transition mode where the Net fluxes are near 0 $\mathrm{W\,m^{-2}}$. The Total flux at the surface for the MOSAiC period based on TCARS, CERES SYN, and observations are 1.7, 15.6, and 3.9 $\mathrm{W\,m^{-2}}$. The over-estimation of the Total flux from CERES SYN is driven by the Sol-N by about 27.4 $\mathrm{W\,m^{-2}}$, whereas the underestimation in the Terr-N accounts for 3.0 $\mathrm{W\,m^{-2}}$. Using the derived surface albedo from CERES SYN and ShupeTurner retrievals (i.e., TCARSe1) suggests an overall overestimation of the Total flux by 13.9 $\mathrm{W\,m^{-2}}$ (Table 6).

Figure 8a illustrates the monthly Terr-N flux at the TOA, showing a consistent annual variation between TCARSe1 and CERES SYN, indicating less negative values of the outgoing terrestrial radiation during Polar night in contrast to Polar day, as more radiation is emitted from the surface and transmitted through the atmosphere to the TOA due to warmer and more humid conditions. The mean Terr-N for TCARSe1 and CERES SYN is -193.6 and -193.7 $\mathrm{W\,m^{-2}}$, respectively (Table 6, Fig. 8b).

The comparison of the Sol-N is depicted in panels c and d of Fig. 8. TCARSe2 calculations exhibit a consistent variation compared to CERES SYN calculations, reaching the highest values in July 2020, and then decreasing in magnitude and variability as a result of decreased surface albedo until September 2020. The mean Sol-N at the TOA for TCARSe2 is 59.7 $\mathrm{W\,m^{-2}}$ whereas for CERES SYN, the mean value is 71.8 $\mathrm{W\,m^{-2}}$, indicating that less solar radiation is absorbed by the atmosphere-surface system in TCARS simulations due to larger atmospheric opacity, which inhibits the solar flux from reaching the surface, thus reducing the Sol-U flux reaching the TOA (see Table 6, Fig. 8d).

At the TOA, the radiation budget is predominantly influenced by the Terr flux for the majority of the MOSAiC period, as depicted in Fig. 8e, with the exceptions being June and July. The net radiation at the TOA, calculated using TCARS and CERES SYN, is -92.7 $\mathrm{W\,m^{-2}}$ and -105.7 $\mathrm{W\,m^{-2}}$, respectively. The discrepancy between these values is primarily attributed to differences in the Sol flux, whereas the Terr fluxes exhibit better agreement.

The calculation of the CRE at the SFC and at the TOA are displayed in Fig. 9 and Fig. 10, respectively. The analysis at the SFC considers the hybrid calculation of the CRE by considering the TCARSe2 cloudless simulations and the observations of upwelling and downwelling Sol and Terr fluxes at ASFS-30 (shown in black in Fig. 9).

https://doi.org/10.5194/egusphere-2024-2193
Preprint. Discussion started: 30 July 2024

The distribution of the Terr CRE shows a decrease of the Terr during Polar night and larger values calculated in October 2019 and from May to September 2020. The annual variation of the Terr CRE is consistent with the findings reported at other sites like the SHEBA (Surface Heat Budget of the Arctic) expedition carried out from 1997 to 1998 north of Alaska (see Fig. 4a in Shupe and Intrieri (2004), Intrieri et al. (2002)), Ny-Ålesund (see Fig. 6c in Ebell et al. (2020)), at the ARM NSA and NOAA Barrow Observatory in Utqiaġvik (see Fig. 3b in Dong et al. (2010)), and in Greenland at Summit Station (72.68°N, 38.58°W) (see Fig. 6b in Miller et al. (2015)).

Additional attention should be given to September 2020 as the largest CERES SYN discrepancies are found during this month. The Terr-D flux is considerably underestimated (Fig. 7a) and does not represent the atmospheric opacity indicated by the other datasets (Fig. 6 m).

The biggest difference among the mentioned sites is that the monthly Terr CRE mean at the two Utqiaġvik sites (Dong et al., 2010) are the lowest in March, with values around 10 $\mathrm{W\,m^{-2}}$, contrasting with the lowest mean values around 30 $\mathrm{W\,m^{-2}}$ calculated in this study and at the other sites. These differences stem from the particular characteristics at each site (Shupe et al., 2011). It is important to note that this comparison aims to provide a general context for the observations at other sites rather than a direct comparison, as the data sampling periods and the amount of data considered differ. Additionally, some discrepancies are due to different references for cloudless situations (Dong et al., 2010).

The calculation of Sol CRE shows a consistent increase in magnitude as there is more solar radiation during June and July 2020 at MOSAiC (Fig. 9c). It is noteworthy that positive values are observed for the hybrid calculations, as broken cloud conditions are not excluded from this analysis. These conditions cannot be simulated within the one-dimensional (1D) radiative transfer setup of TCARS and CERES SYN, hence the values from these models cannot be positive.

Stapf et al. (2020) argued that the calculation of the solar cloud radiative effect should be reassessed by differentiating between the importance of cloudless and all-sky surface albedo. They discuss the applicability of a broadband parameterization that accounts for the presence of liquid clouds. However, future research in this area should also consider the influence of ice and mixed-phase clouds, as well as surface conditions such as pond fraction, fresh snow, white snow, melting snow, and their dependency on the solar zenith angle. A comprehensive investigation into these factors is beyond the scope of the current work.

At the TOA, the variation of the terrestrial cloud radiative effect (Terr CRE) is determined by the cloud top temperature relative to the inversion top temperature. A warming effect is associated with high-level clouds, while a cooling effect occurs when the cloud top temperature is similar to the top atmospheric inversion temperature, a condition more common with mid- and low-level clouds. May and June had the highest cloud occurrence during MOSAiC (Fig. 2), resulting in one of the highest mean Terr CRE values at the TOA, around 10.0 $\mathrm{W\,m^{-2}}$ (Fig. 10a). The mean Terr CRE for the entire MOSAiC period is 6.5 $\mathrm{W\,m^{-2}}$ and 7.0 $\mathrm{W\,m^{-2}}$ for TCARSe2 and CERES SYN, respectively.

The Sol CRE at the TOA shows lower values for TCARSe2 in comparison to CERES SYN. The coolest CRE occurs in July with a mean values of -51.2 and -67 $\mathrm{W\,m^{-2}}$ for TCARSe2 and CERES SYN, respectively (Fig. 10b). The mean Sol CRE for the MOSAiC period is -26.9 $\mathrm{W\,m^{-2}}$ for TCARSe2 and -34.2 $\mathrm{W\,m^{-2}}$ for CERES SYN.

The Net CRE at the SFC and TOA are shown in Fig. 9e, f and Fig. 10e, f, respectively. The time series shows a dominance of warming CRE at the SFC for most of the months except for July 2020 at the SFC and for June, July, and August 2020 at

https://doi.org/10.5194/egusphere-2024-2193
Preprint. Discussion started: 30 July 2024

the TOA. For the entire MOSAiC period, the net CRE at the SFC based on TCARS, CERES SYN and hybrid calculations is 29.3, 26.4, and 25.0 $\mathrm{W\,m^{-2}}$, respectively (Table 6). At the TOA the net CRE is dominated by the cooling effect of -5.2 $\mathrm{W\,m^{-2}}$ based on TCARSe2 calculations and of -8.5 $\mathrm{W\,m^{-2}}$ based on CERES SYN (Table 6, Fig. 10e and f). The latter indicates that during MOSAiC, the atmosphere-surface system loses 5.2 $\mathrm{W\,m^{-2}}$ to space while the surface gains 25.0 $\mathrm{W\,m^{-2}}$ due to the presence of clouds leading to a cooling of the atmosphere by 30.2 $\mathrm{W\,m^{-2}}$.

5 Summary, conclusions and outlook

This study investigated the radiation budget and the cloud radiative effect at the surface and the TOA during the MOSAiC expedition. The analysis included an evaluation of the accuracy of cloud macro- and microphysical retrievals based on a combination of passive and active remote sensing observations and the ShupeTurner algorithm. These retrievals were utilised as input parameters for a one-dimensional (1D) single-column radiative transfer model environment (named TCARS), which uses the RRTMG radiative transfer solver to constrain the radiative impact at the surface and TOA.

The results from the radiative transfer simulations were compared to observations of broadband upwelling and downwelling solar and terrestrial fluxes measured at different stations located over the ice floe and collocated satellite products from CERES SYN Ed. 4. Our results indicate that, in general, there is an overall agreement between the performed radiative transfer simulations, CERES SYN product, and ice floe observations making our analysis sufficient to characterise the radiation budget and investigate the cloud radiative effect during the MOSAiC expedition.

In addition, we evaluated three versions of the TCARS simulations by using different values of surface albedo as input parameters to constrain the surface-cloud interaction and its effect on the Sol-D flux.

Guided by the research questions proposed in the introduction, we summarise our findings and conclude the following:

1. The cloudless TCARS and CERES SYN simulated results exhibit good agreement for Terr and Sol fluxes at both the surface and TOA. The results suggest a consistent correlation across seasons, with correlation coefficients greater than 0.87. However, more notable differences in mean downwelling fluxes are observed for the Sol-D during summer months, displaying a mean flux difference of up to 7.2 $\mathrm{W\,m^{-2}}$. This discrepancy is attributed to aerosol presence, as a comparison using pristine CERES SYN product reduces the bias to -2.0 $\mathrm{W\,m^{-2}}$.

   Overall comparisons between TCARS and MOSAiC flux observations indicate a relatively good agreement for all-sky, cloudy, and cloudless conditions, with median flux differences that do not exceed $\pm$4.8 $\mathrm{W\,m^{-2}}$ for the Terr-D and $\pm$6.8 $\mathrm{W\,m^{-2}}$ for the Sol-D flux.

   The comparison of CERES SYN fluxes to MOSAiC observations also suggests good agreement for Terr-D and Sol-D fluxes, with hourly median flux differences not exceeding 10.2 $\mathrm{W\,m^{-2}}$. However, in contrast to the TCARS results, the CERES SYN comparison displays negative and positive biases for Terr-D and Sol-D fluxes, respectively. This suggests a plausible underestimation of cloud optical thickness, as previously suggested by Huang et al. (2022).

https://doi.org/10.5194/egusphere-2024-2193
Preprint. Discussion started: 30 July 2024

2. Having several ground-based observations of radiative fluxes over the ice floe covering areas of up to approximately 20 km (Cox et al., 2023e) aids the analysis of spatial scale differences between a shipborne measurement and a satellite footprint or grid product. This analysis revealed that the Terr-D flux did not exhibit large variations among Met-City, ASFS-30, ASFS-40, and ASFS-50 observations corroborating the findings in Rabe et al. (2024). On the other hand, other flux components were susceptible to larger differences, especially under cloudless conditions, when the Sol-U fluxes varied by up to 15 $\mathrm{W\,m^{-2}}$. This indicates that the spread among sites was large enough to capture small scale spatiotemporal variability of the surface conditions. Moreover, all of these surface observations were made over sea ice, and thus do not capture the variability of albedo on larger-scales that include some contributions from leads.

3. Evaluating the Net-Terr flux provides an approximation of the atmospheric opacity. During winter, a bimodal distribution is characteristic of the atmospheric conditions, whereas in summer the atmosphere is characterised by optically thick clouds. The comparison of Net-Terr aided in identifying periods during which over/under estimations of cloud opacity led to significant biases for TCARS and CERES SYN product.

   The most significant and recurrent cases in which CERES SYN presented an underestimation of cloud opacity occurred during snowfall events. This is more frequent during the polar night season. Based on detailed analysis, we suspect that CERES SYN misidentifies the cloud base by retrieving cloud temperature much lower than observed during MOSAiC.

   For TCARS results, overestimation of cloud opacity occurred more frequently during geometrically thick ice clouds. It is plausible that the overestimation of cloud opacity is due to overestimation of the cloud ice water content, which might result from the use of retrieval coefficients that were developed for other Arctic locations (Shupe et al., 2005) and may not be optimal for MOSAiC.

4. The surface radiation budget during MOSAiC indicated a clear dominance of the terrestrial flux for most months with the exception of May, June, July and August. A relatively similar distribution of the Terr-N flux is observed for the TCARS, CERES SYN, and MOSAiC observations with values ranging from -20.8 to -28.3 $\mathrm{W\,m^{-2}}$. The mean Sol-N flux for the MOSAiC period ranged from 46.9 to 74.3 $\mathrm{W\,m^{-2}}$. Results of the yearly cycle of the net and downwelling fluxes are comparable to previous results shown in Intrieri et al. (2002), Dong et al. (2010), Miller et al. (2015), and Ebell et al. (2020) for the sites of SHEBA, Summit in Greenland, Alaska, and Ny-Ålesund, respectively.

5. The analysis of the CRE at the surface, based on TCARS, CERES SYN, and a hybrid version using TCARS cloudless simulations and ice-floe observations, indicated relatively good agreement, suggesting a warming effect of clouds at the surface ranging from 19.5 to 30.6 $\mathrm{W\,m^{-2}}$. Throughout the yearly cycle, there is consistent agreement between TCARS and the hybrid Terr CRE calculation. However, during the polar night months, TCARS suggests larger CRE values possibly attributed to an overestimation of atmospheric opacity of geometrically thick ice clouds from ShupeTurner retrievals. CERES SYN product have a similar mean and median Terr CRE as the hybrid calculation, but this is likely compensated by a less humid and colder cloudless atmosphere utilised in CERES SYN to simulate the radiative fluxes at the surface. The overall results are within the same range as previous findings described for annual periods in Intrieri

https://doi.org/10.5194/egusphere-2024-2193
Preprint. Discussion started: 30 July 2024

et al. (2002); Shupe and Intrieri (2004); Dong et al. (2010); Miller et al. (2015); Ebell et al. (2020), but with slightly different characteristics attributed to the atmospheric and surface conditions of each site.

Future work should focus on the variation of surface albedo across scales. Given the sensitivity of radiative fluxes to surface albedo it is important to quantify the spatiotemporal variability from shipborne measurements to satellite footprints, thereby extending the findings presented in this paper and in Huang et al. (2022). Furthermore, we suggest further analysis of the differences in CERES SYN by utilising a reanalysis product that assimilates the radiosondes launched during MOSAiC. It is suspected that the GEOS-5.4.1 reanalysis products may represent a less humid and colder Arctic atmosphere during Polar night. Lastly, this analysis can be deepened by focusing on the atmospheric processes and the relevance of atmospheric heating rates examined with the radiative transfer simulations generated in this study. Our future plans involve broadening the climatological relevance of these findings by considering other Arctic sites such as Ny-Ålesund.

6 Data availability

The analysed ShupeTurner cloud macro and microphysical retrievals can be found in Shupe (2022). Ice-floe observations at Met-City and ASFS-30, ASFS-40 and ASFS-50 stations can be found in Cox et al. (2023a), Cox et al. (2023b), Cox et al. (2023c), and Cox et al. (2023d), respectively. The data used for surface parameters based on single layer hourly ERA5 data is available at Hersbach et al. (2018b) and for pressure levels is available at Hersbach et al. (2018a). The CERES SYN1deg products were obtained from the NASA Langley Research Center Atmospheric Science Data Center, and are available at NASA/LARC/SD/ASDC (2017). All simulations are currently published on Zenodo as three sets of experiments in monthly files. The radiative transfer simulations are published in Barrientos-Velasco (2024).

7 Code and data availability

The radiative transfer simulations based on the model RRTMG model use the Python interface version 0.9.1 available in Deneke (2024).

Author contributions. CBV, HD, AH, and AM conceptualised the manuscript, HD and AM provided supervision. CBV performed the formal analysis, investigation, data curation, methodology, visualisation and writing of the manuscript. MS and CC contributed to the data curation and validation. AM and HD were responsible for the funding acquisition and project administration. All authors contributed to the discussion of the results, subsequent improvement of the analysis, review, and editing of the manuscript.

Competing interests. The authors declare that they have no conflict of interest.

https://doi.org/10.5194/egusphere-2024-2193
Preprint. Discussion started: 30 July 2024

Acknowledgements. We would like to express our gratitude for the funding provided by the Bundesministerium für Bildung und Forschung for the MOSARiCs project (Combining MOSAiC and Satellite Observations for Radiative Closure and Climate Implications) - Project Number 03F0890A, and the Deutsche Forschungsgemeinschaft (DFG, German Research Foundation) - Project Number 268020496 - TRR 172, within the Transregional Collaborative Research Center "ArctiC Amplification: Climate Relevant Atmospheric and Surface Processes, and Feedback Mechanisms $(AC)^3$" during phase III. Data used in this manuscript was produced as part of the international Multidisciplinary drifting Observatory for the Study of the Arctic Climate (MOSAiC) with the tag MOSAiC20192020, therefore we are also deeply thankful to the MOSAiC crew and international scientists for their cooperation and collecting invaluable observations. Additionally, we thank the anonymous reviewers for their suggestions and comments, which significantly improved the final version of this manuscript. A subset of data was obtained from the Atmospheric Radiation Measurement (ARM) User Facility, a U.S. Department of Energy (DOE) Office of Science User Facility Managed by the Biological and Environmental Research Program. We would also like to acknowledge the Copernicus Climate Change Service (C3S) for making their ERA5 products easily accessible. Finally, we extend our appreciation to the NASA Langley Research Center Atmospheric Science Data Center for making their products available for the analysis of this study. Cox and Shupe received support from NOAA's Global Ocean Monitoring and Observing Program (FundRef https://doi.org/10.13039/100018302) and the NOAA Physical Sciences Laboratory. Shupe received additional support from the DOE (DE-SC0021341), National Science Foundation (OPP-1724551), and a Mercator Fellowship with $(AC)^3$.

https://doi.org/10.5194/egusphere-2024-2193
Preprint. Discussion started: 30 July 2024

References

Atlas, D., Matrosov, S. Y., Heymsfield, A. J., Chou, M.-D., and Wolff, D. B.: Radar and Radiation Properties of Ice Clouds, Journal of Applied Meteorology and Climatology, 34, 2329 – 2345, https://doi.org/https://doi.org/10.1175/1520-0450(1995)034<2329:RARPOI>2.0.CO;2, 1995.

Barker, H. W., Stephens, G. L., Partain, P. T., Bergman, J. W., Bonnel, B., Campana, K., Clothiaux, E. E., Clough, S., Cusack, S., Delamere, J., Edwards, J., Evans, K. F., Fouquart, Y., Freidenreich, S., Galin, V., Hou, Y., Kato, S., Li, J., Mlawer, E., Morcrette, J.-J., O'Hirok, W., Räisänen, P., Ramaswamy, V., Ritter, B., Rozanov, E., Schlesinger, M., Shibata, K., Sporyshev, P., Sun, Z., Wendisch, M., Wood, N., and Yang, F.: Assessing 1D Atmospheric Solar Radiative Transfer Models: Interpretation and Handling of Unresolved Clouds, Journal of Climate, 16, 2676–2699, https://doi.org/10.1175/1520-0442(2003)016<2676:ADASRT>2.0.CO;2, 2003.

Barlakas, V., Deneke, H., and Macke, A.: The sub-adiabatic model as a concept for evaluating the representation and radiative effects of low-level clouds in a high-resolution atmospheric model, Atmospheric Chemistry and Physics, 20, 303–322, https://doi.org/10.5194/acp-20-303-2020, 2020.

Barrientos-Velasco, C.: 1D broadband radiative transfer model simulations for the Multidisciplinary drifting Observatory for the Study of Arctic Climate (MOSAiC) expedition, https://doi.org/10.5281/zenodo.12514679, 2024.

Barrientos Velasco, C., Deneke, H., and Macke, A.: Spatial and temporal variability of broadband solar irradiance during POLARSTERN cruise PS106/1 Ice Floe Camp (June 4th-16th 2017), https://doi.org/10.1594/PANGAEA.896710, 2018.

Barrientos-Velasco, C., Deneke, H., Hünerbein, A., Griesche, H. J., Seifert, P., and Macke, A.: Radiative closure and cloud effects on the radiation budget based on satellite and shipborne observations during the Arctic summer research cruise, PS106, Atmospheric Chemistry and Physics, 22, 9313–9348, https://doi.org/10.5194/acp-22-9313-2022, 2022.

Boyer, M., Aliaga, D., Pernov, J. B., Angot, H., Quéléver, L. L. J., Dada, L., Heutte, B., Dall'Osto, M., Beddows, D. C. S., Brasseur, Z., Beck, I., Bucci, S., Duetsch, M., Stohl, A., Laurila, T., Asmi, E., Massling, A., Thomas, D. C., Nøjgaard, J. K., Chan, T., Sharma, S., Tunved, P., Krejci, R., Hansson, H. C., Bianchi, F., Lehtipalo, K., Wiedensohler, A., Weinhold, K., Kulmala, M., Petäjä, T., Sipilä, M., Schmale, J., and Jokinen, T.: A full year of aerosol size distribution data from the central Arctic under an extreme positive Arctic Oscillation: insights from the Multidisciplinary drifting Observatory for the Study of Arctic Climate (MOSAiC) expedition, Atmospheric Chemistry and Physics, 23, 389–415, https://doi.org/10.5194/acp-23-389-2023, 2023.

Cadeddu, M. P., Marchand, R., Orlandi, E., Turner, D. D., and Mech, M.: Microwave Passive Ground-Based Retrievals of Cloud and Rain Liquid Water Path in Drizzling Clouds: Challenges and Possibilities, IEEE Transactions on Geoscience and Remote Sensing, 55, 6468–6481, https://doi.org/10.1109/TGRS.2017.2728699, 2017.

Cesana, G. V., Pierpaoli, O., Ottaviani, M., Vu, L., Jin, Z., and Silber, I.: The correlation between Arctic sea ice, cloud phase and radiation using A-Train satellites, Atmospheric Chemistry and Physics, 24, 7899–7909, https://doi.org/10.5194/acp-24-7899-2024, 2024.

Christensen, M. W., Behrangi, A., L'ecuyer, T. S., Wood, N. B., Lebsock, M. D., and Stephens, G. L.: Arctic Observation and Reanalysis Integrated System: A New Data Product for Validation and Climate Study, Bulletin of the American Meteorological Society, 97, 907–916, https://doi.org/10.1175/BAMS-D-14-00273.1, 2016.

Clough, S., Shephard, M., Mlawer, E., Delamere, J., Iacono, M., Cady-Pereira, K., Boukabara, S., and Brown, P.: Atmospheric radiative transfer modeling: a summary of the AER codes, Journal of Quantitative Spectroscopy and Radiative Transfer, 91, 233 – 244, https://doi.org/https://doi.org/10.1016/j.jqsrt.2004.05.058, 2005.

https://doi.org/10.5194/egusphere-2024-2193
Preprint. Discussion started: 30 July 2024

Collins, W. D., Rasch, P. J., Eaton, B. E., Khattatov, B. V., Lamarque, J.-F., and Zender, C. S.: Simulating aerosols using a chemical transport model with assimilation of satellite aerosol retrievals: Methodology for INDOEX, Journal of Geophysical Research: Atmospheres, 106, 7313–7336, https://doi.org/10.1029/2000JD900507, 2001.

Cox, C., Gallagher, M., Shupe, M., Persson, O., Blomquist, B., Grachev, A., Riihimaki, L., Kutchenreiter, M., Morris, V., Solomon, A., Brooks, I., Costa, D., Gottas, D., Hutchings, J., Osborn, J., Morris, S., Preusser, A., and Uttal, T.: Met City meteorological and surface flux measurements (Level 3 Final), Multidisciplinary Drifting Observatory for the Study of Arctic Climate (MOSAiC), central Arctic, October 2019 - September 2020, Arctic Data Center, https://doi.org/10.18739/A2PV6B83F, 2023a.

Cox, C., Gallagher, M., Shupe, M., Persson, O., Grachev, A., Solomon, A., Ayers, T., Costa, D., Hutchings, J., Leach, J., Morris, S., Osborn, J., Pezoa, S., and Uttal, T.: Atmospheric Surface Flux Station 30 measurements (Level 3 Final), Multidisciplinary Drifting Observatory for the Study of Arctic Climate (MOSAiC), central Arctic, October 2019 - September 2020, Arctic Data Center, https://doi.org/10.18739/A2FF3M18K, 2023b.

Cox, C., Gallagher, M., Shupe, M., Persson, O., Grachev, A., Solomon, A., Ayers, T., Costa, D., Hutchings, J., Leach, J., Morris, S., Osborn, J., Pezoa, S., and Uttal, T.: Atmospheric Surface Flux Station 40 measurements (Level 3 Final), Multidisciplinary Drifting Observatory for the Study of Arctic Climate (MOSAiC), central Arctic, October 2019 - September 2020, Arctic Data Center, https://doi.org/10.18739/A25X25F0P, 2023c.

Cox, C., Gallagher, M., Shupe, M., Persson, O., Grachev, A., Solomon, A., Ayers, T., Costa, D., Hutchings, J., Leach, J., Morris, S., Osborn, J., Pezoa, S., and Uttal, T.: Atmospheric Surface Flux Station 50 measurements (Level 3 Final), Multidisciplinary Drifting Observatory for the Study of Arctic Climate (MOSAiC), central Arctic, October 2019 - September 2020, Arctic Data Center, https://doi.org/10.18739/A2XD0R00S, 2023d.

Cox, C. J., Gallagher, M. R., Shupe, M. D., Persson, P. O. G., Solomon, A., Fairall, C. W., Ayers, T., Blomquist, B., Brooks, I. M., Costa, D., Grachev, A., Gottas, D., Hutchings, J. K., Kutchenreiter, M., Leach, J., Morris, S. M., Morris, V., Osborn, J., Pezoa, S., Preußer, A., Riihimaki, L. D., and Uttal, T.: Continuous observations of the surface energy budget and meteorology over the Arctic sea ice during MOSAiC, Scientific Data, 10, https://doi.org/10.1038/s41597-023-02415-5, 2023e.

D., M. S. and Rex, M.: A Year in the Changing Arctic Sea Ice, Oceanography, https://doi.org/10.5670/oceanog.2022.126, 2022.

Dada, L., Angot, H., Beck, I., and et al.: A central arctic extreme aerosol event triggered by a warm air-mass intrusion, Nat Commun, 13, 5290, https://doi.org/10.1038/s41467-022-32872-2, 2022.

Dahlke, S. and Maturilli, M.: Contribution of Atmospheric Advection to the Amplified Winter Warming in the Arctic North Atlantic Region, Advances in Meteorology, 2017, 1–8, https://doi.org/10.1155/2017/4928620, 2017.

Dahlke, S., Shupe, M. D., Cox, C. J., Brooks, I. M., Blomquist, B., and Persson, P. O. G.: Extended radiosonde profiles 2019/09-2020/10 during MOSAiC Legs PS122/1 - PS122/5, https://doi.org/10.1594/PANGAEA.961881, 2023.

Deneke, H.: hdeneke/pyRRTMG: Release with correct versioning scheme, https://doi.org/10.5281/zenodo.11147087, 2024.

Dong, X., Xi, B., Crosby, K., Long, C. N., Stone, R. S., and Shupe, M. D.: A 10 year climatology of Arctic cloud fraction and radiative forcing at Barrow, Alaska, Journal of Geophysical Research: Atmospheres, 115, https://doi.org/https://doi.org/10.1029/2009JD013489, 2010.

Dong, X., Xi, B., Qiu, S., Minnis, P., Sun-Mack, S., and Rose, F.: A radiation closure study of Arctic stratus cloud microphysical properties using the collocated satellite-surface data and Fu-Liou radiative transfer model, Journal of Geophysical Research: Atmospheres, 121, 10,175–10,198, https://doi.org/10.1002/2016JD025255, 2016.

https://doi.org/10.5194/egusphere-2024-2193
Preprint. Discussion started: 30 July 2024

Duncan, B. N., Ott, L. E., Abshire, J. B., Brucker, L., Carroll, M. L., Carton, J., Comiso, J. C., Dinnat, E. P., Forbes, B. C., Gonsamo, A., Gregg, W. W., Hall, D. K., Ialongo, I., Jandt, R., Kahn, R. A., Karpechko, A., Kawa, S. R., Kato, S., Kumpula, T., Kyrölä, E., Loboda, T. V., McDonald, K. C., Montesano, P. M., Nassar, R., Neigh, C. S., Parkinson, C. L., Poulter, B., Pulliainen, J., Rautiainen, K., Rogers, B. M., Rousseaux, C. S., Soja, A. J., Steiner, N., Tamminen, J., Taylor, P. C., Tzortziou, M. A., Virta, H., Wang, J. S., Watts, J. D., Winker, D. M., and Wu, D. L.: Space-Based Observations for Understanding Changes in the Arctic-Boreal Zone, Reviews of Geophysics, 58, e2019RG000 652, https://doi.org/https://doi.org/10.1029/2019RG000652, e2019RG000652 2019RG000652, 2020.

Dunn, M., Johnson, K., and Jensen, M.: The Microbase Value-Added Product: A Baseline Retrieval of Cloud Microphysical Properties, https://doi.org/10.2172/1015189, 2011.

Dutton, G., Hall, B., Dlugokencky, E., Lan, X., Nance, J., and Madronich, M.: Combined Atmospheric Nitrous Oxide Dry Air Mole Fractions from the NOAA GML Halocarbons Sampling Network, 1977-2023, version: 2023-04-13, https://doi.org/10.15138/GMZ7-2Q16, 2023a.

Dutton, G., Hall, B., Montzka, S., and Nance, J.: Combined Atmospheric Carbon Tetrachloride Dry Air Mole Fractions from the NOAA GML Halocarbons Sampling Network, 1995-2023, version: 2023-04-13, https://doi.org/10.15138/CV0A-J604, 2023b.

Dutton, G., Hall, S., Montzka, J., and Nance, J.: Combined Atmospheric Chlorofluorocarbon-12 Dry Air Mole Fractions from the NOAA GML Halocarbon Sampling Network, 1977-2023, version: 2023-04-13, https://doi.org/10.15138/PJ63-H440, 2023c.

Dutton, G., Hall, S., Montzka, J. D., and Nance, J.: Combined Atmospheric Chlorofluorocarbon-11 Dry Air Mole Fractions from the NOAA GML Halocarbons Sampling Network, 1977-2023, version: 2023-04-13, https://doi.org/10.15138/BVQ6-2S69, 2023d.

Eastman, R. and Warren, S. G.: Arctic Cloud Changes from Surface and Satellite Observations, Journal of Climate, 23, 4233 – 4242, https://doi.org/https://doi.org/10.1175/2010JCLI3544.1, 2010.

Ebell, K., Nomokonova, T., Maturilli, M., and Ritter, C.: Radiative Effect of Clouds at Ny-Ålesund, Svalbard, as Inferred from Ground-Based Remote Sensing Observations, Journal of Applied Meteorology and Climatology, 59, 3–22, https://doi.org/10.1175/JAMC-D-19-0080.1, 2020.

Ebell, K., Walbröl, A., Engelmann, R., Griesche, H., Radenz, M., Hofer, J., and Althausen, D.: Temperature and humidity profiles, integrated water vapour and liquid water path derived from the HATPRO microwave radiometer onboard the Polarstern during the MOSAiC expedition, https://doi.org/10.1594/PANGAEA.941389, 2022.

Fu, Q. and Liou, K. N.: On the Correlated k-Distribution Method for Radiative Transfer in Nonhomogeneous Atmospheres, Journal of the Atmospheric Sciences, 49, 2139–2156, https://doi.org/10.1175/1520-0469(1992)049<2139:OTCDMF>2.0.CO;2, 1992.

Fu, Q. and Liou, K. N.: Parameterization of the Radiative Properties of Cirrus Clouds, Journal of Atmospheric Sciences, 50, 2008 – 2025, https://doi.org/https://doi.org/10.1175/1520-0469(1993)050<2008:POTRPO>2.0.CO;2, 1993.

Fu, Q., Lesins, G., Higgins, J., Charlock, T., Chylek, P., and Michalsky, J.: Broadband water vapor absorption of solar radiation tested using ARM data, Geophysical Research Letters, 25, 1169–1172, https://doi.org/https://doi.org/10.1029/98GL00846, 1998.

Griesche, H. J., Barrientos-Velasco, C., Deneke, H., Hünerbein, A., Seifert, P., and Macke, A.: Low-level Arctic clouds: A blind zone in our knowledge of the radiation budget, EGUsphere, 2023, 1–21, https://doi.org/10.5194/egusphere-2023-358, 2023.

Griesche, H. J., Seifert, P., Engelmann, R., Radenz, M., Hofer, J., Althausen, D., Walbröl, A., Barrientos-Velasco, C., Baars, H., Dahlke, S., Tukiainen, S., and Macke, A.: Cloud micro- and macrophysical properties from ground-based remote sensing during the MOSAiC drift experiment, Scientific Data, 11, 505, https://doi.org/10.1038/s41597-024-03325-w, 2024.

Gu, B.: Evaluations and Improvements of the RRTMG and Fu-Liou Radiative Transfer Model Simulations of Clouds, Doctoral dissertation, Texas A&M University, available electronically from https://hdl.handle.net/1969.1/189047, 2019.

https://doi.org/10.5194/egusphere-2024-2193
Preprint. Discussion started: 30 July 2024

Gupta, S. K., Kratz, D. P., Stackhouse, Paul W., J., Wilber, A. C., Zhang, T., and Sothcott, V. E.: Improvement of Surface Longwave Flux Algorithms Used in CERES Processing, Journal of Applied Meteorology and Climatology, 49, 1579–1589, https://doi.org/10.1175/2010JAMC2463.1, 2010.

Guzman, R., Chepfer, H., Noel, V., Vaillant de Guélis, T., Kay, J. E., Raberanto, P., Cesana, G., Vaughan, M. A., and Winker, D. M.: Direct atmosphere opacity observations from CALIPSO provide new constraints on cloud-radiation interactions, Journal of Geophysical Research: Atmospheres, 122, 1066–1085, https://doi.org/https://doi.org/10.1002/2016JD025946, 2017.

Hartmann, D. L. and Ceppi, P.: Trends in the CERES Dataset, 2000–13: The Effects of Sea Ice and Jet Shifts and Comparison to Climate Models, Journal of Climate, 27, 2444 – 2456, https://doi.org/10.1175/JCLI-D-13-00411.1, 2014.

Heinemann, G., Schefczyk, L., Zentek, R., Brooks, I. M., Dahlke, S., and Walbröl, A.: Evaluation of Vertical Profiles and Atmospheric Boundary Layer Structure Using the Regional Climate Model CCLM during MOSAiC, Meteorology, 2, 257–275, https://doi.org/10.3390/meteorology2020016, 2023.

Herrmannsdörfer, L., Müller, M., Shupe, M. D., and Rostosky, P.: Surface temperature comparison of the Arctic winter MOSAiC observations, ERA5 reanalysis, and MODIS satellite retrieval, Elementa: Science of the Anthropocene, 11, 00085, https://doi.org/10.1525/elementa.2022.00085, 2023.

Hersbach, H., Bell, B., Berrisford, P., Biavati, G., Horányi, A., Muñoz Sabater, J., Nicolas, J., Peubey, C., Radu, R., Rozum, I., Schepers, D., Simmons, A., Soci, C., Dee, D., and Thépaut, J.-N.: ERA5 hourly data on pressure levels from 1979 to present. Copernicus Climate Change Service (C3S) Climate Data Store (CDS)., https://doi.org/10.24381/cds.bd0915c6, accessed on: 02/07/2020, 2018a.

Hersbach, H., Bell, B., Berrisford, P., Biavati, G., Horányi, A., Muñoz Sabater, J., Nicolas, J., Peubey, C., Radu, R., Rozum, I., Schepers, D., Simmons, A., Soci, C., Dee, D., and Thépaut, J.-N.: ERA5 hourly data on single levels from 1979 to present. Copernicus Climate Change Service (C3S) Climate Data Store (CDS)., https://doi.org/10.24381/cds.adbb2d47, accessed on: 17/04/2020, 2018b.

Hersbach, H., Bell, B., Berrisford, P., Hirahara, S., Horányi, A., Muñoz-Sabater, J., Nicolas, J., Peubey, C., Radu, R., Schepers, D., Simmons, A., Soci, C., Abdalla, S., Abellan, X., Balsamo, G., Bechtold, P., Biavati, G., Bidlot, J., Bonavita, M., De Chiara, G., Dahlgren, P., Dee, D., Diamantakis, M., Dragani, R., Flemming, J., Forbes, R., Fuentes, M., Geer, A., Haimberger, L., Healy, S., Hogan, R. J., Hólm, E., Janisková, M., Keeley, S., Laloyaux, P., Lopez, P., Lupu, C., Radnoti, G., de Rosnay, P., Rozum, I., Vamborg, F., Villaume, S., and Thépaut, J.-N.: The ERA5 global reanalysis, Quarterly Journal of the Royal Meteorological Society, 146, 1999–2049, https://doi.org/https://doi.org/10.1002/qj.3803, 2020.

Hu, Y. X. and Stamnes, K.: An Accurate Parameterization of the Radiative Properties of Water Clouds Suitable for Use in Climate Models, Journal of Climate, 6, 728–742, https://doi.org/10.1175/1520-0442(1993)006<0728:AAPOTR>2.0.CO;2, 1993.

Huang, Y., Dong, X., Xi, B., Dolinar, E. K., Stanfield, R. E., and Qiu, S.: Quantifying the Uncertainties of Reanalyzed Arctic Cloud and Radiation Properties Using Satellite Surface Observations, Journal of Climate, 30, 8007–8029, https://doi.org/10.1175/JCLI-D-16-0722.1, 2017.

Huang, Y., Taylor, P. C., Rose, F. G., Rutan, D. A., Shupe, M. D., Webster, M. A., and Smith, M. M.: Toward a more realistic representation of surface albedo in NASA CERES-derived surface radiative fluxes: A comparison with the MOSAiC field campaign: Comparison of CERES and MOSAiC surface radiation fluxes, Elementa: Science of the Anthropocene, 10, 00013, https://doi.org/10.1525/elementa.2022.00013, 2022.

Intrieri, J. M., Fairall, C. W., Shupe, M. D., Persson, P. O. G., Andreas, E. L., Guest, P. S., and Moritz, R. E.: An annual cycle of Arctic surface cloud forcing at SHEBA, Journal of Geophysical Research: Oceans, 107, SHE 13–1–SHE 13–14, https://doi.org/10.1029/2000JC000439, 2002.

https://doi.org/10.5194/egusphere-2024-2193
Preprint. Discussion started: 30 July 2024

Jensen, M., Giangrande, S., Fairless, T., and Zhou, A.: interpolatedsonde, https://doi.org/10.5439/1095316, 1998.

Jin, Z., Charlock, T. P., Smith Jr., W. L., and Rutledge, K.: A parameterization of ocean surface albedo, Geophysical Research Letters, 31, https://doi.org/https://doi.org/10.1029/2004GL021180, 2004.

Johnson, K., Giangrande, S., and Toto, T.: KAZRARSCL-c0-All-inclusive data stream, https://doi.org/10.5439/1393437, 2014.

Jozef, G. C., Cassano, J. J., Dahlke, S., Dice, M., Cox, C. J., and de Boer, G.: Thermodynamic and Kinematic Drivers of Atmospheric Boundary Layer Stability in the Central Arctic during MOSAiC, EGUsphere, 2023, 1–28, https://doi.org/10.5194/egusphere-2023-824, 2023.

Kato, S., Ackerman, T. P., Mather, J. H., and Clothiaux, E. E.: The k-distribution method and correlated-k approximation for a shortwave radiative transfer model, Journal of Quantitative Spectroscopy and Radiative Transfer, 62, 109–121, https://doi.org/https://doi.org/10.1016/S0022-4073(98)00075-2, 1999.

Kato, S., Rose, F. G., and Charlock, T. P.: Computation of Domain-Averaged Irradiance Using Satellite-Derived Cloud Properties, Journal of Atmospheric and Oceanic Technology, 22, 146 – 164, https://doi.org/https://doi.org/10.1175/JTECH-1694.1, 2005.

Kato, S., Loeb, N. G., Rutan, D. A., et al.: Uncertainty Estimate of Surface Irradiances Computed with MODIS-, CALIPSO-, and CloudSat-Derived Cloud and Aerosol Properties, Surveys in Geophysics, 33, 395–412, https://doi.org/10.1007/s10712-012-9179-x, 2012.

Kato, S., Rose, F. G., Rutan, D. A., Thorsen, T. J., Loeb, N. G., Doelling, D. R., Huang, X., Smith, W. L., Su, W., and Ham, S.-H.: Surface Irradiances of Edition 4.0 Clouds and the Earth's Radiant Energy System (CERES) Energy Balanced and Filled (EBAF) Data Product, Journal of Climate, 31, 4501–4527, https://doi.org/10.1175/JCLI-D-17-0523.1, 2018.

Kay, J. E., L'Ecuyer, T., Chepfer, H., Loeb, N., Morrison, A., and Cesana, G.: Recent Advances in Arctic Cloud and Climate Research, Current Climate Change Reports, 2, 159–169, https://doi.org/10.1007/s40641-016-0051-9, 2016.

Key, J.: Streamer user's guide., Tech. Rep., pp. 96–01, 85, https://geocryos.ssec.wisc.edu/streamer/userman.pdf, last access: 15/07/2022, 1996.

Kirbus, B., Tiedeck, S., Camplani, A., Chylik, J., Crewell, S., Dahlke, S., Ebell, K., Gorodetskaya, I., Griesche, H., Handorf, D., Höschel, I., Lauer, M., Neggers, R., Rückert, J., Shupe, M. D., Spreen, G., Walbröl, A., Wendisch, M., and Rinke, A.: Surface impacts and associated mechanisms of a moisture intrusion into the Arctic observed in mid-April 2020 during MOSAiC, Frontiers in Earth Science, 11, https://doi.org/10.3389/feart.2023.1147848, 2023.

Kratz, D. P. and Rose, F. G.: Accounting for Molecular Absorption Within the Spectral Range of the CERES Window Channel, Journal of Quantitative Spectroscopy and Radiative Transfer, 61, 83–95, https://doi.org/https://doi.org/10.1016/S0022-4073(97)00203-3, 1999.

Krumpen, T., von Albedyll, L., Goessling, H., Hendricks, S., Juhls, B., Spreen, G., Willmes, S., Bünger, H. J., Dethloff, K., Haas, C., Kaleschke, L., Katlein, C., Tian-Kunze, X., Ricker, R., Rostosky, P., Rückert, J., Singha, S., and Sokolova, J.: MOSAiC drift expedition from October 2019 to July 2020: Sea ice conditions from space and comparison with previous years, The Cryosphere, 15, 3897–3920, https://doi.org/10.5194/tc-15-3897-2021, 2021.

Lan, X., Dlugokencky, E., Mund, J., Crotwell, A., Crotwell, M., Moglia, E., Madronich, M., Neff, D., and Thoning, K.: Atmospheric Carbon Dioxide Dry Air Mole Fractions from the NOAA GML Carbon Cycle Cooperative Global Air Sampling Network, 1968-2021, version: 2022-11-21, https://doi.org/10.15138/wkgj-f215, 2022a.

Lan, X., Dlugokencky, E., Mund, J., Crotwell, A., Crotwell, M., Moglia, E., Madronich, M., Neff, D., and Thoning, K.: Atmospheric Methane Dry Air Mole Fractions from the NOAA GML Carbon Cycle Cooperative Global Air Sampling Network, 1983-2021, version: 2022-11-21, https://doi.org/10.15138/VNCZ-M766, 2022b.

https://doi.org/10.5194/egusphere-2024-2193
Preprint. Discussion started: 30 July 2024

Lanconelli, C., Busetto, M., Dutton, E. G., König-Langlo, G., Maturilli, M., Sieger, R., Vitale, V., and Yamanouchi, T.: Polar baseline surface radiation measurements during the International Polar Year 2007–2009, Earth System Science Data, 3, 1–8, https://doi.org/10.5194/essd-3-1-2011, 2011.

Lawrence, Z. D., Perlwitz, J., Butler, A. H., Manney, G. L., Newman, P. A., Lee, S. H., and Nash, E. R.: The Remarkably Strong Arctic Stratospheric Polar Vortex of Winter 2020: Links to Record-Breaking Arctic Oscillation and Ozone Loss, Journal of Geophysical Research: Atmospheres, 125, e2020JD033 271, https://doi.org/https://doi.org/10.1029/2020JD033271, e2020JD033271 10.1029/2020JD033271, 2020.

Lelli, L., Vountas, M., Khosravi, N., and Burrows, J. P.: Satellite remote sensing of regional and seasonal Arctic cooling showing a multi-decadal trend towards brighter and more liquid clouds, Atmospheric Chemistry and Physics, 23, 2579–2611, https://doi.org/10.5194/acp-23-2579-2023, 2023.

Light, B., Smith, M., Perovich, D., Webster, M., Holland, M., Linhardt, F., Raphael, I., Clemens-Sewall, D., Macfarlane, A., Anhaus, P., and Bailey, D.: Arctic sea ice albedo: Spectral composition, spatial heterogeneity, and temporal evolution observed during the MOSAiC drift, Elementa: Science of the Anthropocene, 10, https://doi.org/10.1525/elementa.2021.000103, 2022.

López-García, V., Neely, Ryan R., I., Dahlke, S., and Brooks, I. M.: Low-level jets over the Arctic Ocean during MOSAiC, Elementa: Science of the Anthropocene, 10, 00 063, https://doi.org/10.1525/elementa.2022.00063, 2022.

Mace, G. G., Benson, S., and Kato, S.: Cloud radiative forcing at the Atmospheric Radiation Measurement Program Climate Research Facility: 2. Vertical redistribution of radiant energy by clouds, Journal of Geophysical Research: Atmospheres, 111, https://doi.org/https://doi.org/10.1029/2005JD005922, 2006.

Macke, A. and Flores, H.: The Expeditions PS106/1 and 2 of the Research Vessel POLARSTERN to the Arctic Ocean in 2017, Berichte zur Polar- und Meeresforschung, 714, https://doi.org/10.2312/BzPM_0714_2017, last access: 13/07/2022, 2018.

Maturilli, M., Holdridge, D. J., Dahlke, S., Graeser, J., Sommerfeld, A., Jaiser, R., Deckelmann, H., and Schulz, A.: Initial radiosonde data from 2019-10 to 2020-09 during project MOSAiC, https://doi.org/10.1594/PANGAEA.928656, 2021.

Meredith, M., Sommerkorn, M., Cassotta, S., Derksen, C., Ekaykin, A., Hollowed, A., Kofinas, G., Mackintosh, A., Melbourne-Thomas, J., Muelbert, M., Ottersen, G., Pritchard, H., and Schuur, E.: Polar Regions. In: IPCC Special Report on the Ocean and Cryosphere in a Changing Climate, [H.-O. Pörtner, D.C. Roberts, V. Masson-Delmotte, P. Zhai, M. Tignor, E. Poloczanska, K. Mintenbeck, A. Alegría, M. Nicolai, A. Okem, J. Petzold, B. Rama, N.M. Weyer (eds.)]In press., https://www.ipcc.ch/srocc/chapter/chapter-3-2/, last access: 13/07/2022, 2019.

Miller, M. A., Nitschke, K., Ackerman, T. P., Ferrell, W. R., Hickmon, N., and Ivey, M.: The ARM Mobile Facilities, Meteorological Monographs, 57, 9.1 – 9.15, https://doi.org/https://doi.org/10.1175/AMSMONOGRAPHS-D-15-0051.1, 2016.

Miller, N. B., Shupe, M. D., Cox, C. J., Walden, V. P., Turner, D. D., and Steffen, K.: Cloud Radiative Forcing at Summit, Greenland, Journal of Climate, 28, 6267–6280, https://doi.org/10.1175/JCLI-D-15-0076.1, 2015.

Minnis, P., Sun-Mack, S., Chen, Y., Chang, F., Yost, C. R., Smith, W. L., Heck, P. W., Arduini, R. F., Bedka, S. T., Yi, Y., Hong, G., Jin, Z., Painemal, D., Palikonda, R., Scarino, B. R., Spangenberg, D. A., Smith, R. A., Trepte, Q. Z., Yang, P., and Xie, Y.: CERES MODIS Cloud Product Retrievals for Edition 4–Part I: Algorithm Changes, IEEE Transactions on Geoscience and Remote Sensing, 59, 2744–2780, https://doi.org/10.1109/TGRS.2020.3008866, 2021.

Mlawer, E. J., Taubman, S. J., Brown, P. D., Iacono, M. J., and Clough, S. A.: Radiative transfer for inhomogeneous atmospheres: RRTM, a validated correlated-k model for the longwave, Journal of Geophysical Research: Atmospheres, 102, 16 663–16 682, https://doi.org/10.1029/97JD00237, 1997.

https://doi.org/10.5194/egusphere-2024-2193
Preprint. Discussion started: 30 July 2024

Montzka, S.: HCFCs, Halons, Methyl Chloroform, HFC-134a and HFC-152a, https://gml.noaa.gov/hats/data.html, data for individual chemicals can be found at the associated links., 2024.

Morris, V., Zhang, D., and Ermold, B.: ceil, https://doi.org/10.5439/1181954, 1996.

Morrison, H., de Boer, G., Feingold, G., Harrington, J., Shupe, M. D., and Sulia, K.: Resilience of persistent Arctic mixed-phase clouds, Nature Geoscience, 5, 11–17, https://doi.org/10.1038/ngeo1332, 2012.

Murray-Watson, R. J., Gryspeerdt, E., and Goren, T.: Investigating the development of clouds within marine cold-air outbreaks, Atmospheric Chemistry and Physics, 23, 9365–9383, https://doi.org/10.5194/acp-23-9365-2023, 2023.

NASA/LARC/SD/ASDC: CERES and GEO-Enhanced TOA, Within-Atmosphere and Surface Fluxes, Clouds and Aerosols 1-Hourly Terra-Aqua Edition4A, https://doi.org/10.5067/TERRA+AQUA/CERES/SYN1DEG-1HOUR_L3.004A, 2017.

Nicolaus, M., Perovich, D. K., Spreen, G., Granskog, M. A., von Albedyll, L., Angelopoulos, M., Anhaus, P., Arndt, S., Belter, H. J., Bessonov, V., Birnbaum, G., Brauchle, J., Calmer, R., Cardellach, E., Cheng, B., Clemens-Sewall, D., Dadic, R., Damm, E., de Boer, G., Demir, O., Dethloff, K., Divine, D. V., Fong, A. A., Fons, S., Frey, M. M., Fuchs, N., Gabarró, C., Gerland, S., Goessling, H. F., Gradinger, R., Haapala, J., Haas, C., Hamilton, J., Hannula, H.-R., Hendricks, S., Herber, A., Heuzé, C., Hoppmann, M., Høyland, K. V., Huntemann, M., Hutchings, J. K., Hwang, B., Itkin, P., Jacobi, H.-W., Jaggi, M., Jutila, A., Kaleschke, L., Katlein, C., Kolabutin, N., Krampe, D., Kristensen, S. S., Krumpen, T., Kurtz, N., Lampert, A., Lange, B. A., Lei, R., Light, B., Linhardt, F., Liston, G. E., Loose, B., Macfarlane, A. R., Mahmud, M., Matero, I. O., Maus, S., Morgenstern, A., Naderpour, R., Nandan, V., Niubom, A., Oggier, M., Oppelt, N., Pätzold, F., Perron, C., Petrovsky, T., Pirazzini, R., Polashenski, C., Rabe, B., Raphael, I. A., Regnery, J., Rex, M., Ricker, R., Riemann-Campe, K., Rinke, A., Rohde, J., Salganik, E., Scharien, R. K., Schiller, M., Schneebeli, M., Semmling, M., Shimanchuk, E., Shupe, M. D., Smith, M. M., Smolyanitsky, V., Sokolov, V., Stanton, T., Stroeve, J., Thielke, L., Timofeeva, A., Tonboe, R. T., Tavri, A., Tsamados, M., Wagner, D. N., Watkins, D., Webster, M., and Wendisch, M.: Overview of the MOSAiC expedition: Snow and sea ice, Elementa: Science of the Anthropocene, 10, 000 046, https://doi.org/10.1525/elementa.2021.000046, 2022.

NOAA-AGGI: Global Monitoring Laboratory, National Oceanic and Atmospheric Administration (NOAA), https://gml.noaa.gov/aggi/aggi.html, last access: 01/03/2024, 2024.

Pithan, F., Athanase, M., Dahlke, S., Sánchez-Benítez, A., Shupe, M. D., Sledd, A., Streffing, J., Svensson, G., and Jung, T.: Nudging allows direct evaluation of coupled climate models with in situ observations: a case study from the MOSAiC expedition, Geoscientific Model Development, 16, 1857–1873, https://doi.org/10.5194/gmd-16-1857-2023, 2023.

Rabe, B., Heuzé, C., Regnery, J., Aksenov, Y., Allerholt, J., Athanase, M., Bai, Y., Basque, C., Bauch, D., Baumann, T. M., Chen, D., Cole, S. T., Craw, L., Davies, A., Damm, E., Dethloff, K., Divine, D. V., Doglioni, F., Ebert, F., Fang, Y.-C., Fer, I., Fong, A. A., Gradinger, R., Granskog, M. A., Graupner, R., Haas, C., He, H., He, Y., Hoppmann, M., Janout, M., Kadko, D., Kanzow, T., Karam, S., Kawaguchi, Y., Koenig, Z., Kong, B., Krishfield, R. A., Krumpen, T., Kuhlmey, D., Kuznetsov, I., Lan, M., Laukert, G., Lei, R., Li, T., Torres-Valdés, S., Lin, L., Lin, L., Liu, H., Liu, N., Loose, B., Ma, X., McKay, R., Mallet, M., Mallett, R. D. C., Maslowski, W., Mertens, C., Mohrholz, V., Muilwijk, M., Nicolaus, M., O'Brien, J. K., Perovich, D., Ren, J., Rex, M., Ribeiro, N., Rinke, A., Schaffer, J., Schuffenhauer, I., Schulz, K., Shupe, M. D., Shaw, W., Sokolov, V., Sommerfeld, A., Spreen, G., Stanton, T., Stephens, M., Su, J., Sukhikh, N., Sundfjord, A., Thomisch, K., Tippenhauer, S., Toole, J. M., Vredenborg, M., Walter, M., Wang, H., Wang, L., Wang, Y., Wendisch, M., Zhao, J., Zhou, M., and Zhu, J.: Overview of the MOSAiC expedition: Physical oceanography, Elementa: Science of the Anthropocene, 10, 00 062, https://doi.org/10.1525/elementa.2021.00062, 2022.

Rabe, B., Cox, C. J., Fang, Y.-C., Goessling, H., Granskog, M. A., Hoppmann, M., Hutchings, J. K., Krumpen, T., Kuznetsov, I., Lei, R., Li, T., Maslowski, W., Nicolaus, M., Perovich, D., Persson, O., Regnery, J., Rigor, I., Shupe, M. D., Sokolov, V., Spreen, G., Stanton, T.,

https://doi.org/10.5194/egusphere-2024-2193
Preprint. Discussion started: 30 July 2024

Watkins, D. M., Blockley, E., Buenger, H. J., Cole, S., Fong, A., Haapala, J., Heuzé, C., Hoppe, C. J. M., Janout, M., Jutila, A., Katlein, C., Krishfield, R., Lin, L., Ludwig, V., Morgenstern, A., O'Brien, J., Zurita, A. Q., Rackow, T., Riemann-Campe, K., Rohde, J., Shaw, W., Smolyanitsky, V., Solomon, A., Sperling, A., Tao, R., Toole, J., Tsamados, M., Zhu, J., and Zuo, G.: The MOSAiC Distributed Network: Observing the coupled Arctic system with multidisciplinary, coordinated platforms, Elementa: Science of the Anthropocene, 12, 00 103, https://doi.org/10.1525/elementa.2023.00103, 2024.

Rienecker, M. M. . C.: The GOES-5 data assimilation system—documentation of Versions 5.0.1, 5.1.0, and 5.2.0. NASA Tech. Rep. Series on Global Modeling and Data Assimilation NASA/TM-2008-104606, https://ntrs.nasa.gov/citations/20120011955, 2008.

Riihelä, A., Key, J. R., Meirink, J. F., Kuipers Munneke, P., Palo, T., and Karlsson, K.-G.: An intercomparison and validation of satellite-based surface radiative energy flux estimates over the Arctic, Journal of Geophysical Research: Atmospheres, 122, 4829–4848, https://doi.org/10.1002/2016JD026443, 2017.

Riihimaki, L. D., Cronin, M. F., Acharya, R., Anderson, N., Augustine, J., Balmes, K. A., Berk, P., Bozzano, R., Bucholtz, A., Connell, K. J., Cox, C., Di Sarra, A. G., James, E. B., Fairall, C., Farrar, J. T., Grissom, K., Guerra, M. T., Hormann, V., Joseph, K. J., Lanconelli, C., Melin, F., Meloni, D., Ottaviani, M., Pensieri, S., Ramesh, K., Rutan, D., Samarinas, N., Smith, S. R., Swart, S., Tandon, A., Venkatesan, R., Thompson, E., Verma, R. K., Watkins-Brandt, K. S., Weller, R. A., Zappa, C. J., and Zhang, D.: Ocean Surface Radiation Measurement Best Practices, Frontiers, https://doi.org/10.3389/fmars.2024.1359149, 2024.

Rinke, A., Cassano, J. J., Cassano, E. N., Jaiser, R., and Handorf, D.: Meteorological conditions during the MOSAiC expedition: Normal or anomalous?, Elementa: Science of the Anthropocene, 9, 00 023, https://doi.org/10.1525/elementa.2021.00023, 2021.

Rose, F. G., Rutan, D. A., Charlock, T., Smith, G. L., and Kato, S.: An Algorithm for the Constraining of Radiative Transfer Calculations to CERES-Observed Broadband Top-of-Atmosphere Irradiance, Journal of Atmospheric and Oceanic Technology, 30, 1091–1106, https://doi.org/10.1175/JTECH-D-12-00058.1, 2013.

Rossow, W. B. and Zhang, Y.-C.: Calculation of surface and top of atmosphere radiative fluxes from physical quantities based on ISCCP data sets: 2. Validation and first results, Journal of Geophysical Research: Atmospheres, 100, 1167–1197, https://doi.org/https://doi.org/10.1029/94JD02746, 1995.

Rutan, D. A., Kato, S., Doelling, D. R., Rose, F. G., Nguyen, L. T., Caldwell, T. E., and Loeb, N. G.: CERES Synoptic Product: Methodology and Validation of Surface Radiant Flux, Journal of Atmospheric and Oceanic Technology, 32, 1121–1143, https://doi.org/10.1175/JTECH-D-14-00165.1, 2015.

Rückert, J. E., Rostosky, P., Huntemann, M., Clemens-Sewall, D., Ebell, K., Kaleschke, L., Lemmetyinen, J., Macfarlane, A. R., Naderpour, R., Stroeve, J., Walbröl, A., and Spreen, G.: Sea ice concentration satellite retrievals influenced by surface changes due to warm air intrusions: A case study from the MOSAiC expedition, Elementa: Science of the Anthropocene, 11, 00 039, https://doi.org/10.1525/elementa.2023.00039, 2023.

Sassen, K.: Ice Cloud Content from Radar Reflectivity, Journal of Applied Meteorology and Climatology, 26, 1050 – 1053, https://doi.org/https://doi.org/10.1175/1520-0450(1987)026<1050:ICCFRR>2.0.CO;2, 1987.

Serreze, M. C. and Barry, R. G.: Processes and impacts of Arctic amplification: A research synthesis, Global and Planetary Change, 77, 85 – 96, https://doi.org/https://doi.org/10.1016/j.gloplacha.2011.03.004, 2011.

Shupe, M. D.: A ground-based multisensor cloud phase classifier, Geophysical Research Letters - GEOPHYS RES LETT, 34, https://doi.org/10.1029/2007GL031008, 2007.

Shupe, M. D.: ShupeTurner cloud microphysics, https://doi.org/10.5439/1871015, 2022.

https://doi.org/10.5194/egusphere-2024-2193
Preprint. Discussion started: 30 July 2024

Shupe, M. D. and Intrieri, J. M.: Cloud Radiative Forcing of the Arctic Surface: The Influence of Cloud Properties, Surface Albedo, and Solar Zenith Angle, Journal of Climate, 17, 616–628, https://doi.org/10.1175/1520-0442(2004)017<0616:CRFOTA>2.0.CO;2, 2004.

Shupe, M. D., Uttal, T., and Matrosov, S. Y.: Arctic Cloud Microphysics Retrievals from Surface-Based Remote Sensors at SHEBA, Journal of Applied Meteorology, 44, 1544–1562, https://doi.org/10.1175/JAM2297.1, 2005.

Shupe, M. D., Walden, V. P., Eloranta, E., Uttal, T., Campbell, J. R., Starkweather, S. M., and Shiobara, M.: Clouds at Arctic Atmospheric Observatories. Part I: Occurrence and Macrophysical Properties, Journal of Applied Meteorology and Climatology, 50, 626–644, https://doi.org/10.1175/2010JAMC2467.1, 2011.

Shupe, M. D., Turner, D. D., Zwink, A., Thieman, M. M., Mlawer, E. J., and Shippert, T.: Deriving Arctic Cloud Microphysics at Barrow, Alaska: Algorithms, Results, and Radiative Closure, Journal of Applied Meteorology and Climatology, 54, 1675–1689, https://doi.org/10.1175/JAMC-D-15-0054.1, 2015.

Shupe, M. D., Rex, M., Dethloff, K., Damm, E., Fong, A. A., Gradinger, R., Heuzé, C., Loose, B., Makarov, A., Maslowski, W., Nicolaus, M., Perovich, D., Rabe, B., Rinke, A., Sokolov, V., and Sommerfeld, A.: Arctic report card 2020: The MOSAiC expedition: A year drifting with the arctic sea ice, 2020.

Shupe, M. D., Rex, M., Blomquist, B., Persson, P. O. G., Schmale, J., Uttal, T., Althausen, D., Angot, H., Archer, S., Bariteau, L., Beck, I., Bilberry, J., Bucci, S., Buck, C., Boyer, M., Brasseur, Z., Brooks, I. M., Calmer, R., Cassano, J., Castro, V., Chu, D., Costa, D., Cox, C. J., Creamean, J., Crewell, S., Dahlke, S., Damm, E., de Boer, G., Deckelmann, H., Dethloff, K., Dütsch, M., Ebell, K., Ehrlich, A., Ellis, J., Engelmann, R., Fong, A. A., Frey, M. M., Gallagher, M. R., Ganzeveld, L., Gradinger, R., Graeser, J., Greenamyer, V., Griesche, H., Griffiths, S., Hamilton, J., Heinemann, G., Helmig, D., Herber, A., Heuzé, C., Hofer, J., Houchens, T., Howard, D., Inoue, J., Jacobi, H.-W., Jaiser, R., Jokinen, T., Jourdan, O., Jozef, G., King, W., Kirchgaessner, A., Klingebiel, M., Krassovski, M., Krumpen, T., Lampert, A., Landing, W., Laurila, T., Lawrence, D., Lonardi, M., Loose, B., Lüpkes, C., Maahn, M., Macke, A., Maslowski, W., Marsay, C., Maturilli, M., Mech, M., Morris, S., Moser, M., Nicolaus, M., Ortega, P., Osborn, J., Pätzold, F., Perovich, D. K., Petäjä, T., Pilz, C., Pirazzini, R., Posman, K., Powers, H., Pratt, K. A., Preußer, A., Quéléver, L., Radenz, M., Rabe, B., Rinke, A., Sachs, T., Schulz, A., Siebert, H., Silva, T., Solomon, A., Sommerfeld, A., Spreen, G., Stephens, M., Stohl, A., Svensson, G., Uin, J., Viegas, J., Voigt, C., von der Gathen, P., Wehner, B., Welker, J. M., Wendisch, M., Werner, M., Xie, Z., and Yue, F.: Overview of the MOSAiC expedition: Atmosphere, Elementa: Science of the Anthropocene, 10, 00 060, https://doi.org/10.1525/elementa.2021.00060, 2022.

Sivaraman, C., Flynn, D., Riihimaki, L., Comstock, J., and Zhang, D.: Cloud Mask from Micropulse Lidar, https://doi.org/10.5439/1508389, 2019.

Solomon, A., Shupe, M. D., Svensson, G., Barton, N. P., Batrak, Y., Bazile, E., Day, J. J., Doyle, J. D., Frank, H. P., Keeley, S., Remes, T., and Tolstykh, M.: The winter central Arctic surface energy budget: A model evaluation using observations from the MOSAiC campaign, Elementa: Science of the Anthropocene, 11, 00 104, https://doi.org/10.1525/elementa.2022.00104, 2023.

Stapf, J., Ehrlich, A., Jäkel, E., Lüpkes, C., and Wendisch, M.: Reassessment of shortwave surface cloud radiative forcing in the Arctic: consideration of surface-albedo–cloud interactions, Atmospheric Chemistry and Physics, 20, 9895–9914, https://doi.org/10.5194/acp-20-9895-2020, 2020.

Stubenrauch, C. J., Rossow, W. B., Kinne, S., Ackerman, S., Cesana, G., Chepfer, H., Girolamo, L. D., Getzewich, B., Guignard, A., Heidinger, A., Maddux, B. C., Menzel, W. P., Minnis, P., Pearl, C., Platnick, S., Poulsen, C., Riedi, J., Sun-Mack, S., Walther, A., Winker, D., Zeng, S., and Zhao, G.: Assessment of Global Cloud Datasets from Satellites: Project and Database Initiated by the GEWEX Radiation Panel, Bulletin of the American Meteorological Society, 94, 1031 – 1049, https://doi.org/10.1175/BAMS-D-12-00117.1, 2013.

https://doi.org/10.5194/egusphere-2024-2193
Preprint. Discussion started: 30 July 2024

Svensson, G., Murto, S., Shupe, M. D., Pithan, F., Magnusson, L., Day, J. J., Doyle, J. D., Renfrew, I. A., Spengler, T., and Vihma, T.: Warm air intrusions reaching the MOSAiC expedition in April 2020—The YOPP targeted observing period (TOP), Elementa: Science of the Anthropocene, 11, 00 016, https://doi.org/10.1525/elementa.2023.00016, 2023.

Tan, I. and Storelvmo, T.: Evidence of Strong Contributions From Mixed-Phase Clouds to Arctic Climate Change, Geophysical Research Letters, 46, 2894–2902, https://doi.org/10.1029/2018GL081871, 2019.

Taylor, P. C., Boeke, R. C., Boisvert, L. N., Feldl, N., Henry, M., Huang, Y., Langen, P. L., Liu, W., Pithan, F., Sejas, S. A., and Tan, I.: Process Drivers, Inter-Model Spread, and the Path Forward: A Review of Amplified Arctic Warming, Frontiers in Earth Science, 9, https://doi.org/10.3389/feart.2021.758361, 2022.

Taylor, P. C., Langen, P. L., and Tan, I.: Editorial: Arctic amplification: Feedback process interactions and contributions, Frontiers in Earth Science, 11, https://doi.org/10.3389/feart.2023.1140871, 2023.

Uttal, T., Starkweather, S., Drummond, J. R., Vihma, T., Makshtas, A. P., Darby, L. S., Burkhart, J. F., Cox, C. J., Schmeisser, L. N., Haiden, T., Maturilli, M., Shupe, M. D., Boer, G. D., Saha, A., Grachev, A. A., Crepinsek, S. M., Bruhwiler, L., Goodison, B., McArthur, B., Walden, V. P., Dlugokencky, E. J., Persson, P. O. G., Lesins, G., Laurila, T., Ogren, J. A., Stone, R., Long, C. N., Sharma, S., Massling, A., Turner, D. D., Stanitski, D. M., Asmi, E., Aurela, M., Skov, H., Eleftheriadis, K., Virkkula, A., Platt, A., Førland, E. J., Iijima, Y., Nielsen, I. E., Bergin, M. H., Candlish, L., Zimov, N. S., Zimov, S. A., O'Neill, N. T., Fogal, P. F., Kivi, R., Konopleva-Akish, E. A., Verlinde, J., Kustov, V. Y., Vasel, B., Ivakhov, V. M., Viisanen, Y., and Intrieri, J. M.: International Arctic Systems for Observing the Atmosphere: An International Polar Year Legacy Consortium, Bulletin of the American Meteorological Society, 97, 1033 – 1056, https://doi.org/10.1175/BAMS-D-14-00145.1, 2016.

Wang, M., Johnson, K., and Giangrande, S.: arsclwacr1kolliasshp.c0, https://doi.org/10.5439/1823070, 2022.

Webster, M. A., Holland, M., Wright, N. C., Hendricks, S., Hutter, N., Itkin, P., Light, B., Linhardt, F., Perovich, D. K., Raphael, I. A., Smith, M. M., von Albedyll, L., and Zhang, J.: Spatiotemporal evolution of melt ponds on Arctic sea ice: MOSAiC observations and model results, Elementa: Science of the Anthropocene, 10, 000 072, https://doi.org/10.1525/elementa.2021.000072, 2022.

Wendisch, M., Macke, A., Ehrlich, A., Lüpkes, C., Mech, M., Chechin, D., Dethloff, K., Velasco, C. B., Bozem, H., Brückner, M., Clemen, H.-C., Crewell, S., Donth, T., Dupuy, R., Ebell, K., Egerer, U., Engelmann, R., Engler, C., Eppers, O., Gehrmann, M., Gong, X., Gottschalk, M., Gourbeyre, C., Griesche, H., Hartmann, J., Hartmann, M., Heinold, B., Herber, A., Herrmann, H., Heygster, G., Hoor, P., Jafariserajehlou, S., Jäkel, E., Järvinen, E., Jourdan, O., Kästner, U., Kecorius, S., Knudsen, E. M., Köllner, F., Kretzschmar, J., Lelli, L., Leroy, D., Maturilli, M., Mei, L., Mertes, S., Mioche, G., Neuber, R., Nicolaus, M., Nomokonova, T., Notholt, J., Palm, M., van Pinxteren, M., Quaas, J., Richter, P., Ruiz-Donoso, E., Schäfer, M., Schmieder, K., Schnaiter, M., Schneider, J., Schwarzenböck, A., Seifert, P., Shupe, M. D., Siebert, H., Spreen, G., Stapf, J., Stratmann, F., Vogl, T., Welti, A., Wex, H., Wiedensohler, A., Zanatta, M., and Zeppenfeld, S.: The Arctic Cloud Puzzle: Using ACLOUD/PASCAL Multiplatform Observations to Unravel the Role of Clouds and Aerosol Particles in Arctic Amplification, Bulletin of the American Meteorological Society, 100, 841–871, https://doi.org/10.1175/BAMS-D-18-0072.1, 2019.

Wilber, A., Kratz, D., and Gupta, S.: Surface Emissivity Maps for Use in Retrievals of Longwave Radiation Satellite, https://www-calipso.larc.nasa.gov/resources/calipso_users_guide/data_summaries/pdfs/Wilber.NASATchNote99.pdf, last access: 01/10/2020, 1999.

Witthuhn, J., Hünerbein, A., Filipitsch, F., Wacker, S., Meilinger, S., and Deneke, H.: Aerosol properties and aerosol–radiation interactions in clear sky conditions over Germany, Atmospheric Chemistry and Physics Discussions, 2021, 1–64, https://doi.org/10.5194/acp-2021-517, 2021.

https://doi.org/10.5194/egusphere-2024-2193
Preprint. Discussion started: 30 July 2024

Węglarczyk, Stanisław: Kernel density estimation and its application, ITM Web Conf., 23, 00 037, https://doi.org/10.1051/itmconf/20182300037, 2018.

Zhang, D.: mwrret1liljclou, https://doi.org/10.5439/1027369, 1996.

Zib, B. J., Dong, X., Xi, B., and Kennedy, A.: Evaluation and Intercomparison of Cloud Fraction and Radiative Fluxes in Recent Reanalyses over the Arctic Using BSRN Surface Observations, Journal of Climate, 25, 2291–2305, https://doi.org/10.1175/JCLI-D-11-00147.1, 2012.

https://doi.org/10.5194/egusphere-2024-2193
Preprint. Discussion started: 30 July 2024

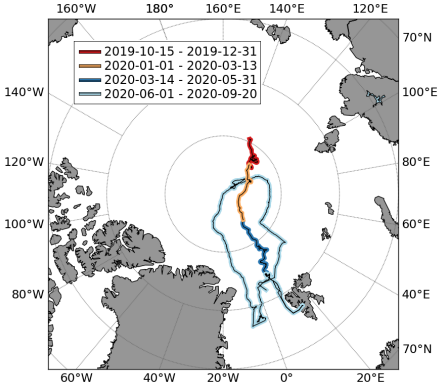

Figure 1. The cruise track of the research vessel Polarstern during the MOSAiC expedition is shown on an Arctic polar stereographic map. The red and orange solid lines show the track during the polar night, and the blue and light blue solid lines denote the track during the polar day. Each colour represents the period shown in the upper box discussed in Section 4.2.

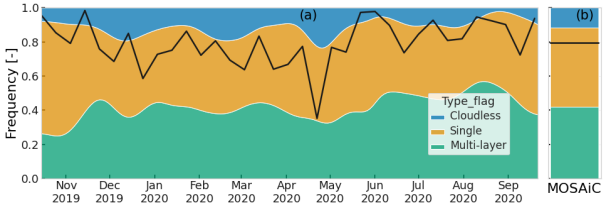

Figure 2. Time series showing the occurrence and composition of clouds during MOSAiC. Panel a shows the occurrence frequency of cloudless conditions (blue), single-layer clouds (orange), and multi-layer clouds (green), while the black line shows the cloud fraction from CERES SYN. The black line in panel a shows the 10-day averaged normalised cloud area fraction from CERES SYN, and mean values are shown in the black solid line in panel b.

https://doi.org/10.5194/egusphere-2024-2193
Preprint. Discussion started: 30 July 2024

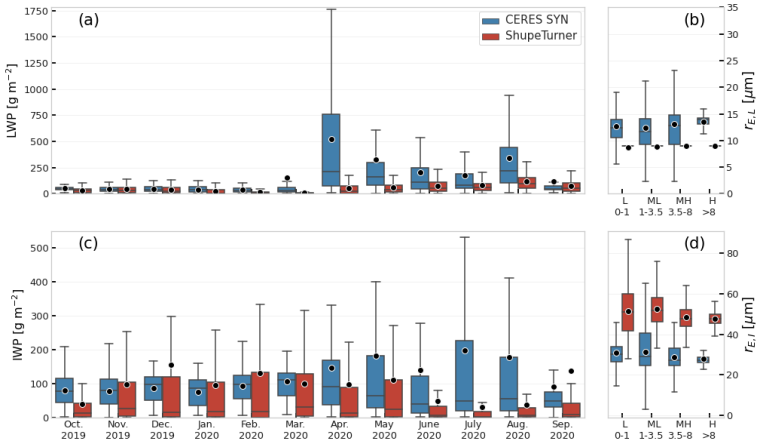

Figure 3. Time series of cloud water paths based on the ShupeTurner and CERES SYN retrievals. Panels a and c show box plots of monthly statistics of the liquid water path (LWP) and ice water path (IWP), respectively for the CERES SYN (blue) and ShupeTurner (red) datasets. Panels b and d show statistics of the vertical profiles of liquid droplet ($r_{E,L}$) and ice crystals ($r_{E,I}$) effective radius for low-level (L; 0-1 km), mid-low level (ML; 1-3.5 km), mid-high level (MH; 3.5-8 km), and high-level clouds (H; >8 km) for the entire MOSAiC expedition. Boxes in panels c-f extend from the 25th to 75th percentile, the median is represented by a line, and the black dots depict the mean.

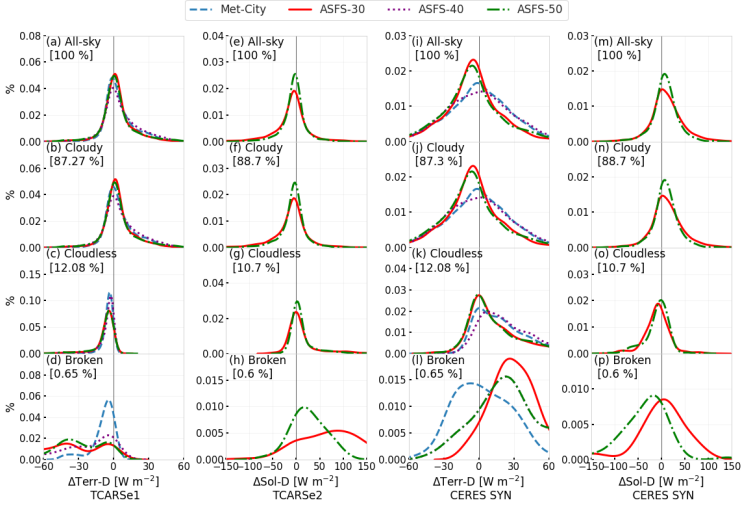

Figure 4. Kernel density estimate (KDE) of the distribution of differences between simulated and observed radiative fluxes at the surface. The first two columns show the KDE for the TCARS simulations, while the last two columns show the KDE for CERES SYN collocated to the positions of Met-City, ASFS-30, ASFS-40, and ASFS-50.

https://doi.org/10.5194/egusphere-2024-2193
Preprint. Discussion started: 30 July 2024

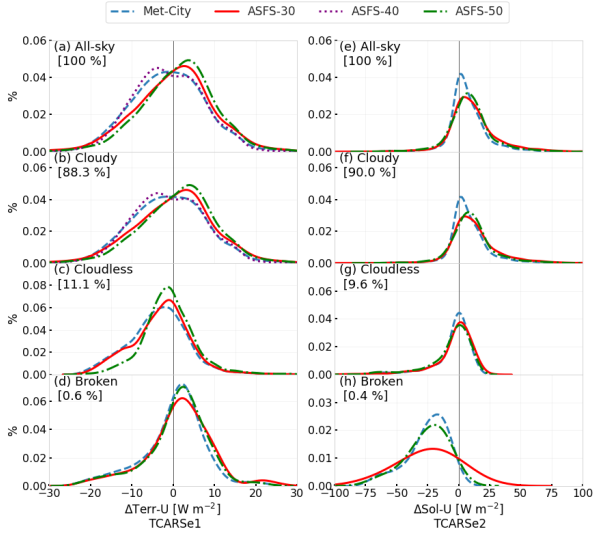

Figure 5. Same as Figure 4, but comparing the KDE of the difference between TCARS and CERES SYN fluxes at the TOA. TCARSe1 simulations are considered for the Terr-U and TCARSe2 for the Sol-U comparison.

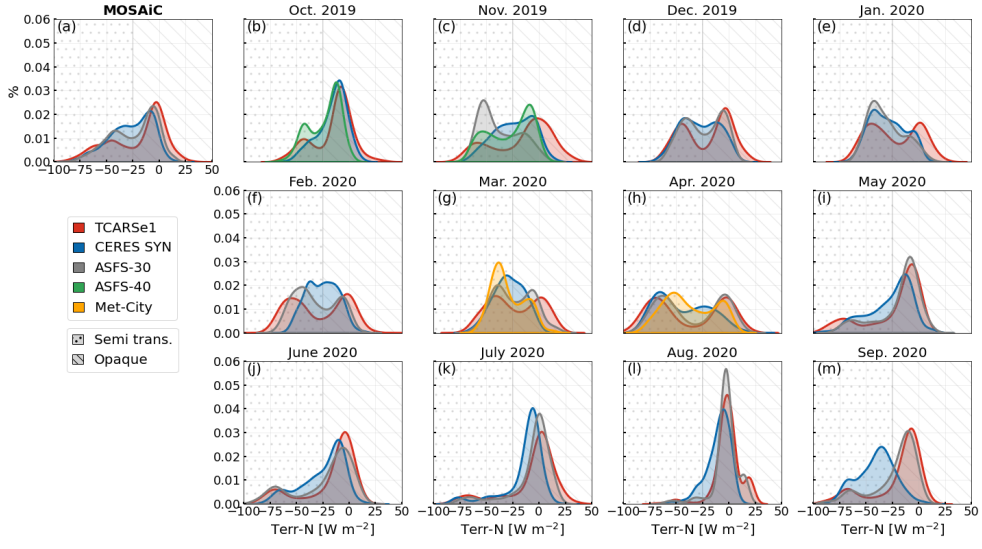

Figure 6. Monthly distributions of net terrestrial flux (Terr-N) for TCARSe1 simulations, CERES SYN product and observations at the ASFS-30 station. For October and November 2019, an additional comparison is shown with observations at ASFS-40, and for March and April 2020, the Terr-N distributions at Met-City are included. Note that the distributions in November 2019 and September 2020 represent 15 and 20 days, respectively.

https://doi.org/10.5194/egusphere-2024-2193
Preprint. Discussion started: 30 July 2024

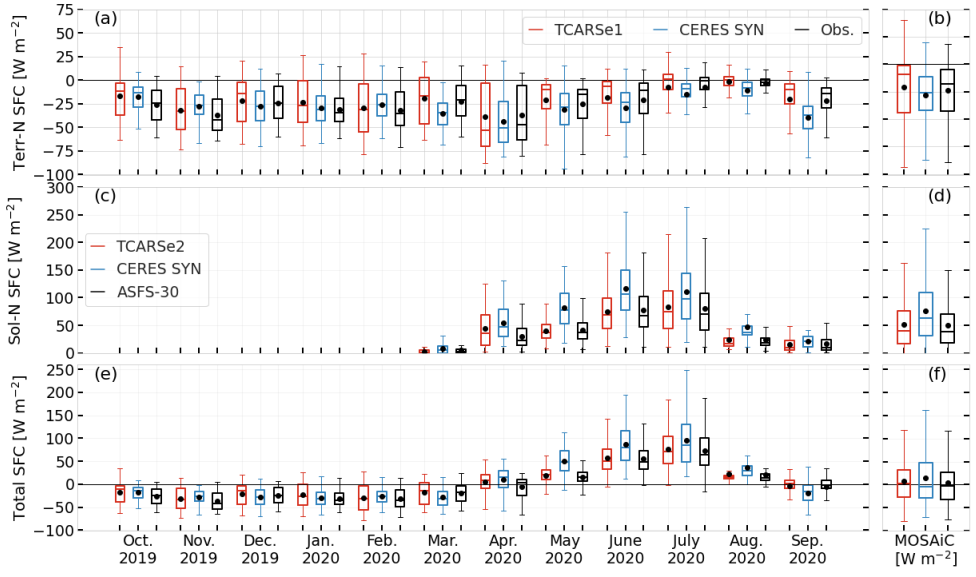

Figure 7. Time series of terrestrial (panels a,b) and solar flux (panels c,d) at the surface for TCARS simulations, CERES SYN product, and observations at the ASFS-30 station and Met-City for the last 15 days of October 2019. Panels e and f show the net radiation budget at the surface (SFC). Panels b, d and f show the mean values for the entire MOSAiC period. The box plot shows the distribution of the net fluxes. Panel d shows the statistical values for the period when solar radiation is available during MOSAiC. The mean values for the entire MOSAiC expedition are indicated in Table 6.

https://doi.org/10.5194/egusphere-2024-2193
Preprint. Discussion started: 30 July 2024

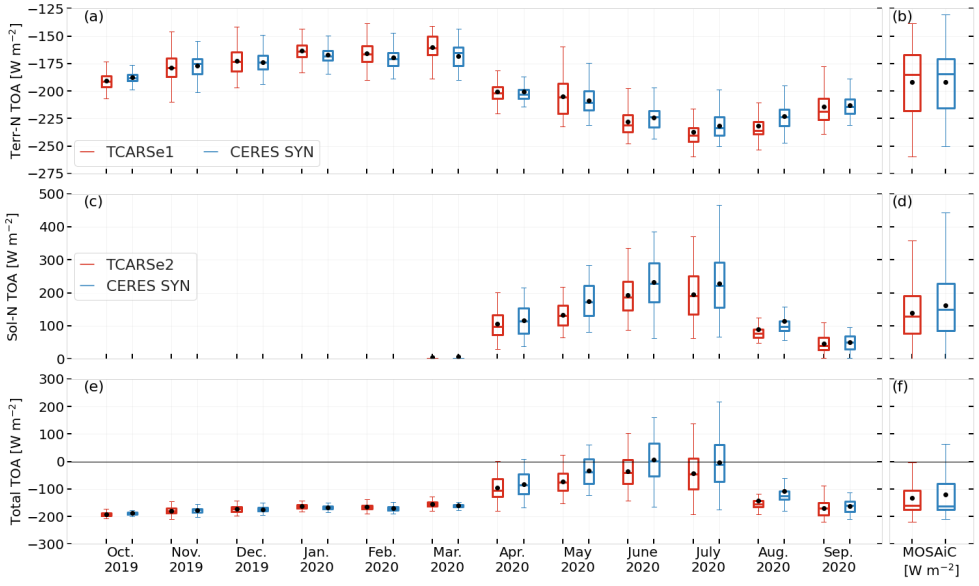

Figure 8. Time series shown as monthly box plots for the net terrestrial (Terr-N, panels a and b), net solar (Sol-N, panels c and d), and total flux at the top of the atmosphere (Net, panels e and f). The box plots for TCARS are displayed in red, while the ones for CERES SYN are shown in blue. Box plots for the entire MOSAiC period are displayed in panels b, d, and f. Panel d shows the statistical values for the period when solar radiation is available during MOSAiC. The mean values for the entire MOSAiC expedition are indicated in Table 6.

Figure 9. Time series of monthly box plots for the terrestrial (panel a), solar (panel b), and total (panel c) cloud radiative effect (CRE) at the surface. Box plots for the entire MOSAiC period are shown in panels b, d, and f. Panel d shows the statistical values for the period when solar radiation is available during MOSAiC. The mean values for the entire MOSAiC expedition are indicated in Table 6.

https://doi.org/10.5194/egusphere-2024-2193
Preprint. Discussion started: 30 July 2024

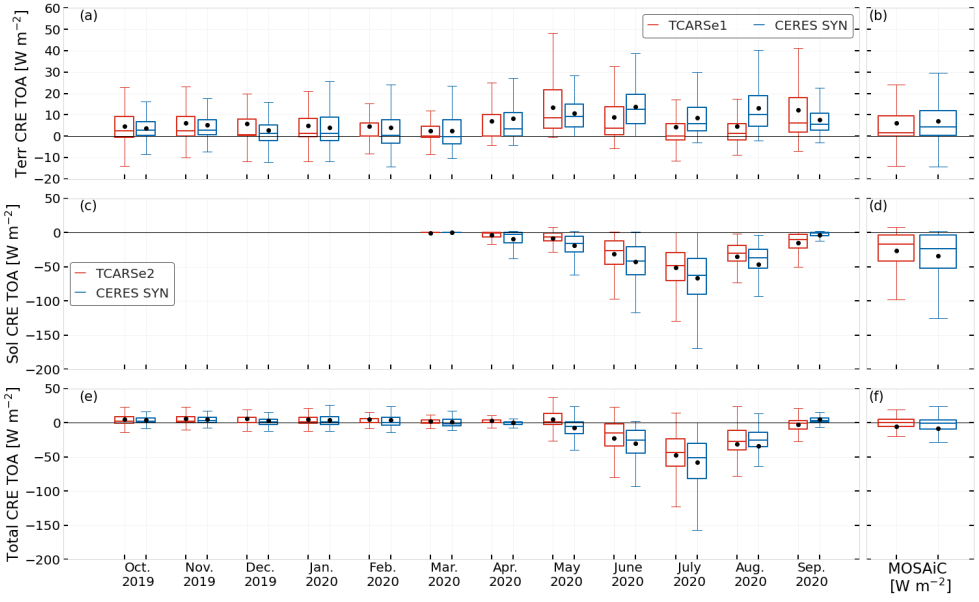

Figure 10. Time series of monthly box plots of the terrestrial (panel a), solar (panel b), and net (panel c) cloud radiative effect (CRE) at the TOA. Box plots for the entire MOSAiC period are shown in panels b, d, and f. Panel d shows the statistical values for the period when solar radiation is available during MOSAiC. The mean values for the entire MOSAiC expedition are indicated in Table 6.

https://doi.org/10.5194/egusphere-2024-2193
Preprint. Discussion started: 30 July 2024

Table 1. List of data sources for ShupeTurner retrievals as well as for the radiative transfer simulations (TCARS), and for supplementary analysis (SA).

	Instruments/Dataset	Measurements	References
ShupeTurner	Micropulse lidar (MPL)	Backscatter and depolarization ratio	Sivaraman et al. (2019)
	Ceilometer	Cloud base	Morris et al. (1996)
	Ka-band ARM Zenith Radar (KAZR)	Doopler radar, reflectivity, spectra Best estimates of cloud boundaries	Johnson et al. (2014) Wang et al. (2022)
	Radiosondes	Interpolation of atmospheric properties	Jensen et al. (1998)
	MiRAC-P radiometer	Liquid water path	Ebell et al. (2022)
	ARM Microwave radiometer	Liquid water path	Zhang (1996)
TCARS	ShupeTurner	Cloud properties	Shupe (2022)
	ERA5	Atmospheric pressure, temperature, specific humidity, ozone, and surface pressure	Hersbach et al. (2020)
	NOAA Annual Greenhouse Gas Index (AGGI)	CO mole fraction CO_2 mole fraction CH_4 mole fraction N_2O mole fraction CCl_4 mole fraction CFC-12 mole fraction CFC-11 mole fraction HCFC-22 mole fraction	NOAA-AGGI (2024) Lan et al. (2022a) Lan et al. (2022b) Dutton et al. (2023a) Dutton et al. (2023b) Dutton et al. (2023c) Dutton et al. (2023d) Montzka (2024)
	ASFS-30	Skin temperature Daily mean surface albedo	Cox et al. (2023b) Cox et al. (2023b)
	ASFS-50	Daily mean surface albedo	Cox et al. (2023d)
	CERES SYN	Surface albedo and ice fraction	Rutan et al. (2015)
SA	Met-City ASFS-30 ASFS-40 ASFS-50 Radiosondes	Skin temperature, radiative fluxes Skin temperature, radiative fluxes Skin temperature, radiative fluxes Skin temperature, radiative fluxes Blend products of atmospheric properties	Cox et al. (2023a) Cox et al. (2023b) Cox et al. (2023c) Cox et al. (2023d) Dahlke et al. (2023)

https://doi.org/10.5194/egusphere-2024-2193
Preprint. Discussion started: 30 July 2024

Table 2. Hourly downwelling terrestrial flux difference (FD) at the surface (SFC) for the entire MOSAiC period under different atmospheric conditions in $\mathrm{W\,m^{-2}}$. Results are based on TCARS simulations, CERES SYN product (CERES), and observations at ASFS-30. An additional comparison for CERES SYN cloudless (CS) products is given for cloudless and broken cloud conditions.

Atm. Cond.		All-sky		Cloudy		Cloudless		Broken	
FD		TCARSe1	CERES	TCARSe1	CERES	TCARSe1	CERES (CS)	TCARSe1	CERES (CS)
Terr-D (SFC)	Mean	3.2	-4.4	3.9	-4.9	-8.0	13.2 (-9.9)	-32.7	4.8 (-38.3)
	Median	1.8	-4.7	2.2	-5.2	-4.8	6.5 (-6.2)	-36.5	1.6 (-42.0)
	RMSE	14.0	24.5	14.2	24.4	13.9	25.6 (17.3)	40.7	25.9 (45.0)
	SD	13.6	24.1	13.6	23.9	11.3	21.9 (14.2)	24.2	25.4 (21.2)

Table 3. Hourly downwelling solar (Sol-D) flux difference (FD) at the surface (SFC) for the entire MOSAiC period under different atmospheric conditions in $\mathrm{W\,m^{-2}}$. Results are shown for CERES SYN (CERES) products, TCARS simulations using different surface albedo based on CERES SYN surface albedo (TCARSe1), daily mean from observations at ASFS-30 (TCARSe2), and at ASFS50 (TCARSe3). An additional comparison for CERES SYN cloudless (CS) products is given for cloudless and broken cloud conditions.

Atm. Cond.		All-sky				Cloudy			
FD		TCARSe1	TCARSe2	TCARSe3	CERES	TCARSe1	TCARSe2	TCARSe3	CERES
Sol-D (SFC)	Mean	-11.8	-1.7	3.9	12.3	-13.4	4.0	4.8	13.0
	Median	-5.9	-1.0	1.8	9.4	-6.8	1.7	3.5	10.2
	RMSE	45.7	41.6	35.6	39.3	46.3	39.4	41.2	39.6
	SD	44.1	41.5	35.4	37.3	44.3	39.2	40.9	37.4
Atm. Cond.		Cloudless				Broken			
FD		TCARSe1	TCARSe2	TCARSe3	CERES (CS)	TCARSe1	TCARSe2	TCARSe3	CERES (CS)
Sol-D (SFC)	Mean	12.4	14.6	19.3	-10.2 (7.3)	75.4	82.3	77.0	-3.0 (59.7)
	Median	1.3	3.3	5.0	-8.3 (-0.5)	76.9	83.8	78.8	7.6 (54.9)
	RMSE	37.7	39.3	42.9	33.2 (33.9)	102.2	108.3	97.0	57.5 (91.0)
	SD	35.6	36.5	38.3	31.6 (33.0)	69.0	70.5	58.9	57.4 (61.7)

https://doi.org/10.5194/egusphere-2024-2193
Preprint. Discussion started: 30 July 2024

Table 4. Hourly radiative flux difference (FD) at the top-of-the-atmosphere (TOA) for the entire MOSAiC period under different atmospheric conditions. Results are based on TCARS simulations and CERES SYN observations in $\mathrm{W\,m^{-2}}$.

Atm. Cond.		All-sky	Cloudy	Cloudless	Broken
FD		TCARSe1	TCARSe1	TCARSe1	TCARSe1
Terr-U (TOA)	Mean	0.3	0.4	-2.8	1.5
	Median	0.7	0.9	-2.3	2.0
	RMSE	9.6	9.7	7.7	8.0
	SD	9.6	9.7	7.1	7.9

Table 5. Hourly upwelling solar (Sol-U) flux difference (FD) at the top-of-the-atmosphere (TOA) for the entire MOSAiC period under different atmospheric conditions in $\mathrm{W\,m^{-2}}$. Results are shown for CERES SYN (CERES) products, TCARS simulations using different surface albedo based on CERES SYN surface albedo (TCARSe1), daily mean from observations at ASFS-30 (TCARSe2), and at ASFS50 (TCARSe3). An additional comparison for CERES SYN cloudless (CS) products is given for cloudless and broken cloud conditions.

Atm. Cond.		All-sky			Cloudy		
FD		TCARSe1	TCARSe2	TCARSe3	TCARSe1	TCARSe2	TCARSe3
Sol-U (TOA)	Mean	11.4	26.8	22.7	12.4	26.8	22.5
	Median	8.9	20.8	17.4	9.6	21.0	17.5
	RMSE	23.7	38.4	35.2	23.9	38.2	34.7
	SD	20.8	27.5	26.9	20.4	27.2	26.4
Atm. Cond.		Cloudless sky			Broken		
FD		TCARSe1	TCARSe2	TCARSe3	TCARSe1	TCARSe2	TCARSe3
Sol-U (TOA)	Mean	-4.0	21.0	17.0	-35.6	36.3	30.6
	Median	0.0	10.4	8.2	-22.8	21.6	14.4
	RMSE	18.9	39.9	38.9	61.2	56.3	55.2
	SD	18.4	34.0	35.0	49.7	43.0	45.9

https://doi.org/10.5194/egusphere-2024-2193
Preprint. Discussion started: 30 July 2024

Table 6. Mean hourly values of the radiation budget during MOSAiC in W m^{-2}. Values in parentheses indicate the standard deviation (SD). The percentage is given for the temporal coverage of the available simulations for MOSAiC. The calculations of the observations (Obs.) are based mostly on ASFS-30 observations except for October 2019, when the observations at Met-City are considered due to temporal coverage. Two calculations are considered for CERES SYN, the first one for 100 % temporal coverage as in TCARSe1 and then for 97.2 % of the same temporal coverage as TCARSe2 simulations.

Data		TCARSe1	TCARSe2	TCARSe3	CERES SYN	CERES SYN	Obs.
Percentage		100 %	97.2 %	76.5 %	100 %	97.2 %	97.2 %
TOA	Terr-N	-193.6 (30.2)	-192.0 (20.1)	-188.2 (29.1)	-193.7 (25.7)	-192.1 (25.9)	-
	Sol-N	71.3 (96.2)	59.7 (85.9)	41.8 (76.1)	71.9 (102.5)	71.8 (103.2)	-
	Total	-122.3 (77.1)	-132.4 (65.7)	-146.0 (57.5)	-120.4 (83.0)	-120.4 (83.4)	-
	CRE	-15.5 (40.0)	-5.2 (24.8)	-3.3 (23.2)	-8.3 (27.5)	-8.5 (27.6)	-
SFC	Terr-N	-21.1 (26.7)	-20.8 (26.5)	-22.0 (26.7)	-28.3 (20.6)	-26.7 (19.9)	-23.7 (22.7)
	Sol-N	64.0 (60.0)	50.2 (45.5)	50.4 (49.0)	72.2 (57.9)	74.3 (58.0)	46.9 (43.8)
	Total	17.8 (58.7)	1.7 (44.9)	1.1 (46.7)	15.6 (59.1)	15.9 (59.6)	3.9 (46.2)
	CRE	19.5 (41.1)	29.3 (32.8)	30.6 (33.2)	22.8 (31.8)	26.4 (31.8)	25.0 (32.4)

https://doi.org/10.5194/egusphere-2024-2193
Preprint. Discussion started: 30 July 2024

Appendix A: Temporal coverage of radiative transfer simulations

Figure A1 illustrates the temporal coverage of the different radiative transfer experiments created with TCARS.

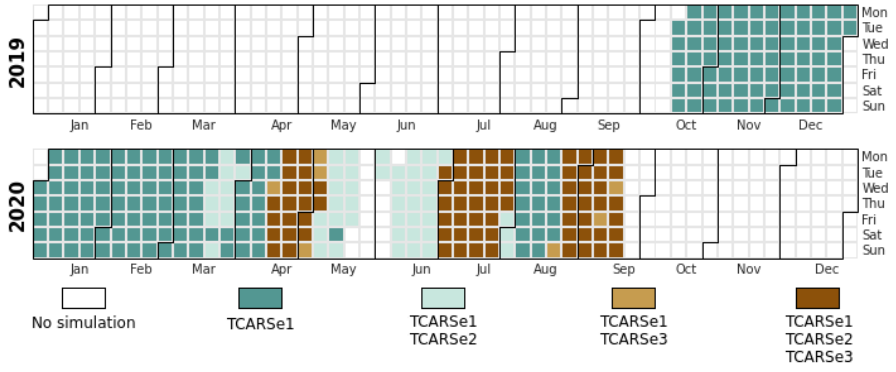

Figure A1. Calendar showing the temporal coverage of each experimental set of TCARS simulations for the MOSAiC period from 2019-10-15 to 2020-09-20.

Appendix B: Atmospheric and Surface conditions

The atmospheric temperature during MOSAiC is illustrated in Fig. B1 based on ERA5 atmospheric profiles and the blended product from Dahlke et al. (2023) to illustrate the variation of this parameter in K.

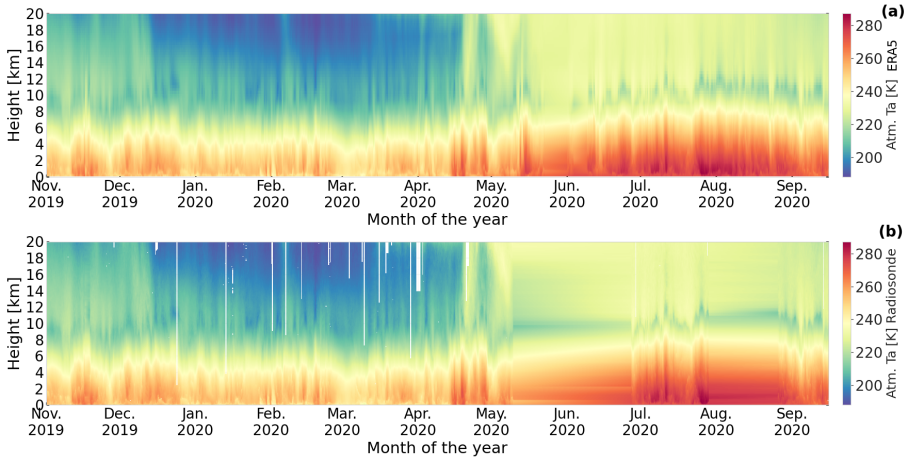

Figure B1. Time series of linearly interpolated atmospheric temperature for MOSAiC based on ERA5 (panel a), and merged radiosondes (panel b).

https://doi.org/10.5194/egusphere-2024-2193
Preprint. Discussion started: 30 July 2024

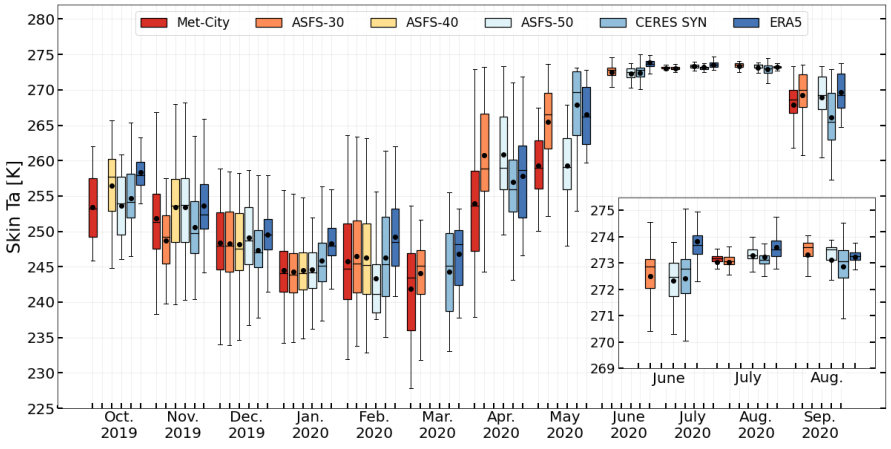

Figure B2. Monthly time series of box plots showing the distribution of skin temperature for MOSAiC based on ERA5, CERES SYN, and ice floe stations.

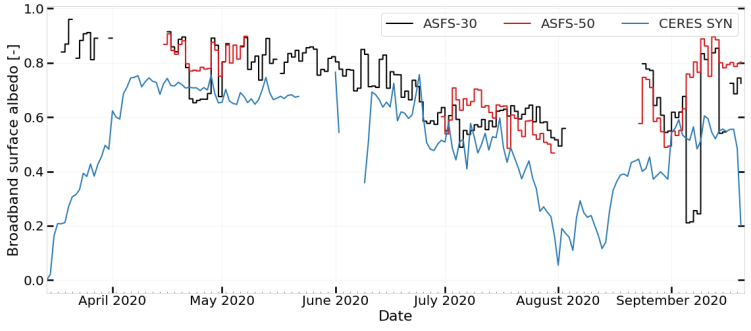

Figure B3. Time series of the daily mean broadband surface albedo from 2020-03-14 to 2020-09-20. Data gaps in the CERES SYN time series are subject to the overall data availability for the radiative transfer simulations.

Appendix C: Comparison of cloudless simulations

In all the plots of this section, the first row indicates the distribution of the Kernel Density Estimate (KDE) of the flux difference between TCARSe1 simulations minus CERES SYN product, and the second row presents the linear regression of each comparison. The KDE is a technique utilised to estimate the probability density function (PDF) from a collection of data points, producing a smooth estimate of the PDF. The shape of the KDE indicates the concentration of data points within the sample dataset (Węglarczyk, Stanisław, 2018).

https://doi.org/10.5194/egusphere-2024-2193
Preprint. Discussion started: 30 July 2024

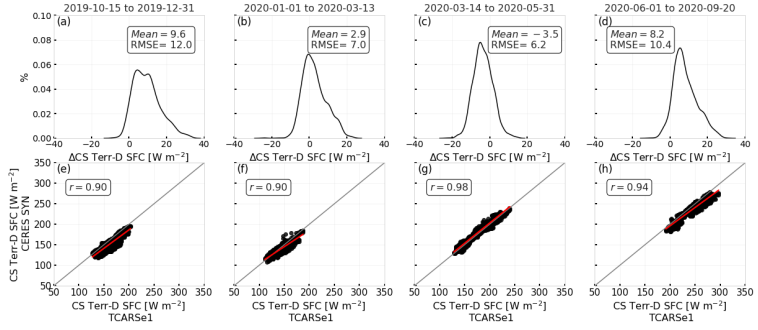

Figure C1. Comparison of downwelling terrestrial radiative flux (Terr-D) at the surface for cloudless simulations between TCARS and CERES SYN: The first row shows the kernel density distribution of TCARS minus CERES SYN fluxes. The second row shows scatter plots comparing CERES SYN (y-axis) and TCARS simulations (x-axis). Linear regressions are shown by the red line. Mean, RMSE and correlation coefficient are indicated in each box. Each column depicts the results for each period indicated in the top panel.

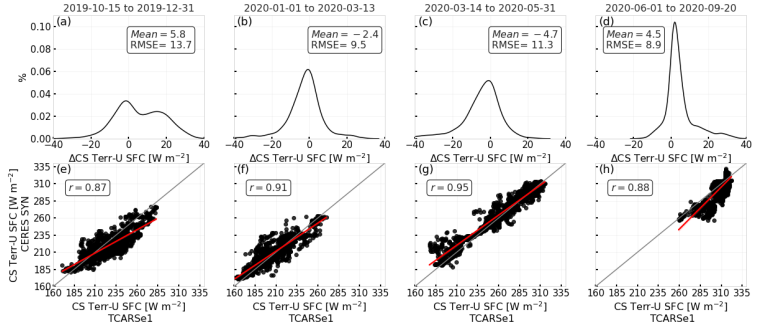

Figure C2. Same as Fig. C1, but for the upwelling terrestrial flux (Terr-U) at the surface.

https://doi.org/10.5194/egusphere-2024-2193
Preprint. Discussion started: 30 July 2024

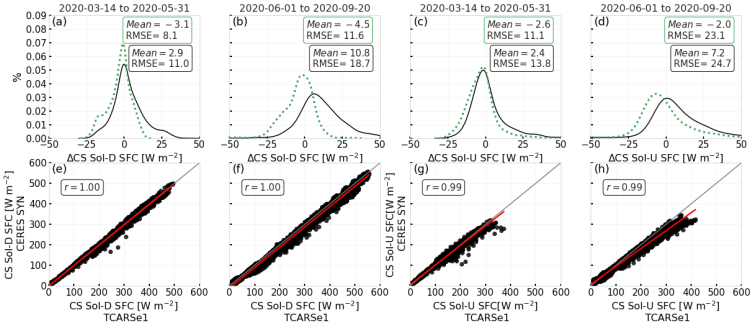

Figure C3. Comparison of downwelling solar radiative flux (Sol-D; panel a,b,e, and f) and upwelling solar radiative flux (Sol-U; panel c, d, g, and h) at the surface for cloudless simulations between TCARS and CERES SYN: The first row shows the kernel density estimate (KDE) distribution of TCARS minus CERES SYN fluxes. The second row shows scatter plots comparing CERES SYN (y-axis) and TCARS simulations (x-axis). Linear regressions are shown by the red line. Mean, RMSE and correlation coefficient are indicated in each box. Each column depicts the results for each period indicated in the top panel. The green dotted KDE distribution shown in panels a-d show the same comparison for CERES SYN fluxes for pristine conditions.

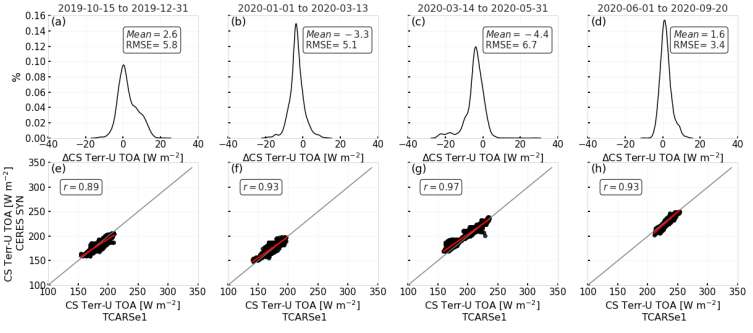

Figure C4. Same as Fig. C2, but for the TOA.

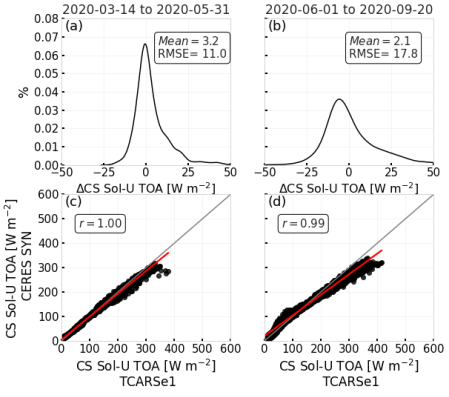

Figure C5. Similar to panels c, d, g, and h, but for the TOA in Fig. C3.

https://doi.org/10.5194/egusphere-2024-2193
Preprint. Discussion started: 30 July 2024

Appendix D: Radiative flux difference for all available ice floe stations during MOSAiC

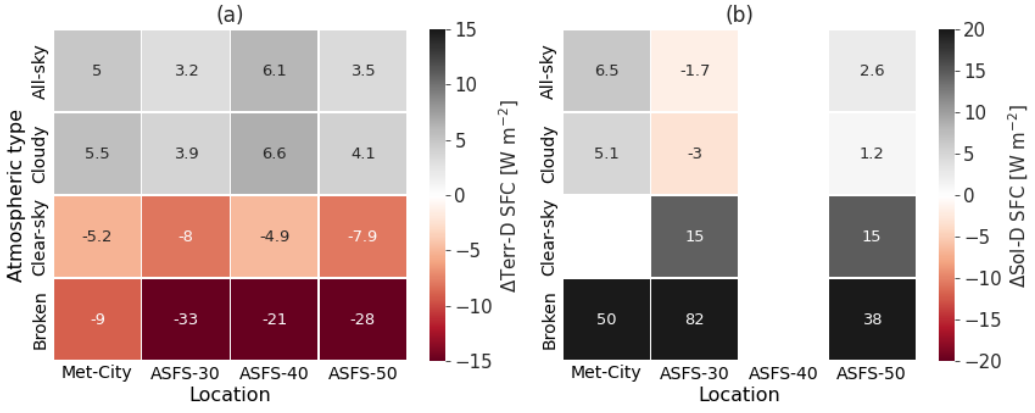

Figure D1. Mean flux difference between TCARSe1 simulations and observed broadband radiative fluxes for MOSAiC at the surface (SFC). Panel (a) and (b) show downwelling Terrestrial (Terr-D) and Solar (Sol-D) fluxes, respectively for all stations.

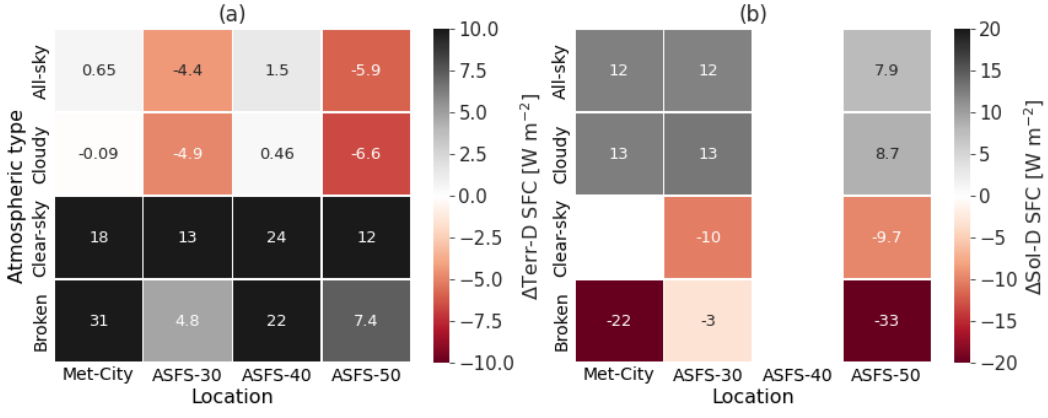

Figure D2. Same as Fig. D1 but comparing CERES SYN minus observations.

https://doi.org/10.5194/egusphere-2024-2193
Preprint. Discussion started: 30 July 2024

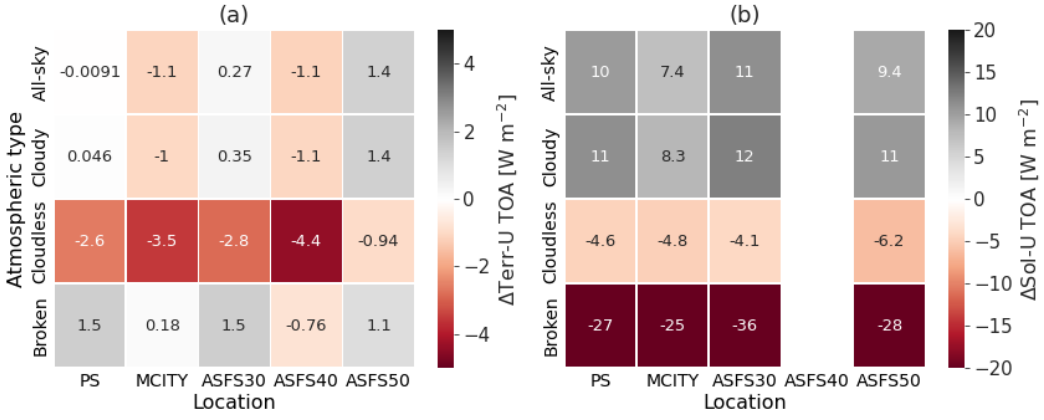

Figure D3. Mean flux difference between TCARS and CERES SYN fluxes at the TOA. Panel (a) shows biases for the upwelling terrestrial flux (Terr-U) considering TCARSe1, and (b) shows the comparison for the upwelling solar flux (Sol-U) using TCARSe2.

https://doi.org/10.5194/egusphere-2024-2193
Preprint. Discussion started: 30 July 2024

Table A1. List of Acronyms

Abbreviation	Meaning
AGGI	Annual Greenhouse Gas Index
Atm.	Atmospheric
ASFS	Atmospheric Surface Flux Stations
CERES	Clouds and the Earth's Radiant Energy System
CERES SYN	Clouds and the Earth's Radiant Energy System SYN Ed.4.1 product
Cond.	Conditions
CS	Cloudless
CRE	Cloud Radiative Effect
Eff.	Effective
FD	Flux difference
KDE	Kernel Density Estimate
LWC	Liquid water content
LWP	Liquid water path
MOSAiC	Multidisciplinary drifting Observatory for the Study of Arctic Climate
IWC	Ice water content
IWP	Ice water path
Obs.	Observations
PS	*Polarstern*
$r_{E,L}$	Liquid droplet effective radius
$r_{E,I}$	Ice crystal effective radius
RMSE	Root mean squared error
RRTMG	Rapid radiative transfer model (RRTM) for GCM applications
SFC	Surface
SO	Surface Observatory
Sol-D	Broadband downwelling solar flux
Sol-N	Broadband net solar flux
Sol-U	Broadband upwelling solar flux
SD	Standard Deviation
TCARS	TROPOS Cloud and Aerosol Radiative effect Simulator
Terr-D	Broadband downwelling terrestrial flux
Terr-N	Broadband net terrestrial flux
Terr-U	Broadband upwelling terrestrial flux
TOA	Top of the atmosphere

https://doi.org/10.5194/egusphere-2024-2193
Preprint. Discussion started: 30 July 2024

Table A2. Hourly radiative flux difference (FD) between simulated (TCARSe1) and observed downwelling fluxes at surface (SFC) and upwelling fluxes at the top-of-the-atmosphere (TOA) for single-layer clouds subdivided by cloud phase for the entire MOSAiC period in $\mathrm{W\,m^{-2}}$. The flux comparison at the surface considers observations at the ASFS-30 station and the TOA products from CERES SYN.

Atm. Cond.		Liquid	Ice	Mixed
FD		TCARSe1	TCARSe1	TCARSe1
Terr-U (TOA)	Mean	7.4	-2.8	0.6
	Median	6.4	-3.0	2.1
	RMSE	11.0	8.9	10.8
	SD	8.2	8.4	10.8
Terr-D (SFC)	Mean	3.8	-1.4	7.3
	Median	2.7	-2.4	4.0
	RMSE	16.0	21.6	16.2
	SD	15.6	21.5	14.4

Table A3. The hourly radiative flux difference (FD) between TCARS and observations is measured in $\mathrm{W\,m^{-2}}$. At the surface (SFC), downwelling fluxes are compared, while at the top-of-the-atmosphere (TOA), solar upwelling fluxes are analysed. These comparisons are conducted for single-layer clouds, which are further subdivided by cloud phase, over the entire MOSAiC period. Surface observations are obtained from the ASFS-30 station, and TOA observations are sourced from CERES SYN data. TCARS simulations using different surface albedo based on CERES SYN surface albedo (e1), daily mean from observations at ASFS-30 (e2), and at ASFS50 (e3).

Atm. Cond.		Liquid			Ice			Mixed		
FD		e1	e2	e3	e1	e2	e3	e1	e2	e3
Sol-U (TOA)	Mean	14.6	34.2	31.2	-3.4	15.9	8.5	16.6	29.1	22.3
	Median	11.6	27.4	23.7	0.0	10.8	5.7	13.1	22.8	17.6
	RMSE	29.6	45.7	44.0	20.8	32.8	28.8	26.0	39.2	32.0
	SD	25.8	30.3	31.1	20.4	28.6	27.5	20.0	26.2	23.0
Sol-D (SFC)	Mean	-11.6	0.8	3.1	17.6	21.7	20.0	-20.8	-8.4	0.6
	Median	-6.3	1.6	3.3	2.6	4.9	6.5	-8.3	-2.3	-1.1
	RMSE	57.4	55.3	51.9	52.8	56.4	49.4	54.6	47.5	28.7
	SD	56.3	55.3	51.8	49.8	52.1	45.2	50.5	46.7	28.7